Bruno Dall'Agnol de Oliveira

O impacto da retro-alimentação de Buracos Negros Supermassivos nas suas galáxias hospedeiras (*Gauging the effect of feedback from Supermassive Black Holes on the host galaxies*)

Porto Alegre

Março de 2020

Bruno Dall'Agnol de Oliveira

O impacto da retro-alimentação de Buracos Negros Supermassivos nas suas galáxias hospedeiras (*Gauging the effect of feedback from Supermassive Black Holes on the host galaxies*)

Dissertação de Mestrado apresentada ao Programa de Pós-Graduação em Física da Universidade Federal do Rio Grande do Sul, como requisito parcial para obtenção do grau de Mestrado em Física: Astrofísica.

Universidade Federal do Rio Grande do Sul - UFRGS

Instituto de Física

Departamento de Astronomia

Orientadora: Thaisa Storchi Bergmann

Porto Alegre

Março de 2020

Agradecimentos

À toda a minha famíia, pela presença e por todo o amor recebido ao longo desses anos.

À minha orientadora Thaisa, pelo apoio e orientação que recebi desde a minha Graduação.

Às demais pessoas e bichos, que me acompanharam nessa trajetória, alegrando os meus dias.

Ao Conselho Nacional de Desenvolvimento Científico e Tecnológico (CNPq), pelo suporte financeiro.

Resumo

Frequentemente associados à regulação da formação estelar nos núcleos galácticos ativos (AGN), os buracos negros supermassivos (SMBH) desempenham um papel fundamental na evolução das galáxias através de seus efeitos de *feedback* (retro-alimentação). Para investigar o impacto deste *feedback* no modo radiativo – causado por fótons energéticos durante o processo de acreção de matéria – analisamos, em um trabalho anterior, imagens de banda estreita obtidas com o *Hubble Space Telescope* (HST) de uma amostra de nove AGNs do tipo II com luminosidades bolométricas $L_{Bol} > 10^{45}\,erg\,s^{-1}$, no qual encontramos que o gás emissor de linhas estreitas (ENLR) se estende além do corpo da galáxia, sugerindo um *feedback* poderoso do AGN através da ejeção de gás a grandes distâncias do núcleo. No entanto, para verificar se há mesmo ejeção de gás nesses objetos, e quantificar o seu efeito sobre a galáxia, precisamos mapear a cinemática do gás, e assim calcular a taxa de ejeção de massa e a sua potência cinética. Para isto, observamos parte de nossa amostra usando observações de espectroscopia de campo integral com o instrumento Gemini GMOS-IFU, num total de oito objetos. A cinemática do gás foi obtida através do ajuste de componentes Gaussianas aos perfis das linhas de emissão do gás ionizado. Em geral, além de uma componente larga (*broad*), foram necessárias mais de duas componentes estreitas (*narrow*) para representar os perfis da NLR. Encontramos que a cinemática das componentes *narrow* é bem complexa, condizente com a presença de interações com galáxias vizinhas, previamente observado nas imagens do HST. Associamos a componente *broad* ao gás em *outflow*: esta componente possui valores de dispersão de velocidade de até $850\,km\,s^{-1}$, o que reforça a identificação dessa componente com o gás perturbado em ejeção. Utilizando apenas a componente *broad*, calculamos a taxa de massa de gás ionizado em *outflow* ($\dot{M}_{out}$), encontrando valores de até $10\,M_{\odot}\,yr^{-1}$. A potência cinética do *outflow* ($\dot{E}_{out}$) atinge valores máximos entre 10^{41} e $10^{43}\,erg\,s^{-1}$, o que corresponde a eficiências de *feedback* de $\sim 0.001 - 0.1\,\%$ da L_{Bol}. Estes valores estão abaixo dos encontrados em simulações e modelos analíticos que reproduzem os efeitos da cessação da formação estelar durante a evolução das galáxias. Entretanto, nossos cálculos consideram somente a contribuição ao *outflow* do gás ionizado, que representa apenas uma fração da energia liberada pelo *feedback*. Investigamos também a relação de $\dot{M}_{out}$ e $\dot{E}_{out}$ com L_{Bol}, e o efeito das incertezas em algumas grandezas – como a densidade e a massa total do gás ionizado em outflow – nos valores finais de $\dot{M}_{out}$ e $\dot{E}_{out}$.

Palavras-chave: Galáxias Ativas. Quasares. Retro-alimentação. Linhas de emissão. Buracos Negros Supermassivos.

Abstract

Often associated with the regulation of star formation in active galactic nuclei (AGN), supermassive black holes (SMBH) play a fundamental role in the evolution of galaxies through their feedback effects. To investigate the impact of this feedback in the radiative mode – caused by energetic photons during the process of accretion of matter – we analyzed, in a previous work, narrow-band images obtained with Hubble Space Telescope (HST) of a sample of nine type II AGNs with bolometric luminosities $L_{Bol} > 10^{45}\,erg\,s^{-1}$. There, we found that the gas emitting narrow lines (ENLR) extends beyond the body of the galaxy, suggesting a powerful AGN feedback through gas ejection to large distances from the nucleus. However, to check if there is even an outflow in these objects, and to quantify its effect on the galaxy, we need to map the gas kinematics, and then calculate the mass outflow rate and its kinetic power. For this, we observed part of our sample using integral field spectroscopy observations with the Gemini GMOS-IFU instrument, for a total of eight objects. The gas kinematics was obtained by fitting Gaussian components to the profiles of the emission lines of the ionized gas. In general, in addition to a *broad* component, more than two *narrow* components were required to represent the NLR profiles. We found that the kinematics of the *narrow* components are quite complex, consistent with the presence of interactions with nearby galaxies, previously observed in the HST images. We associate the *broad* component with the gas in outflow: this component has velocity dispersion values up to $850\,km\,s^{-1}$, which reinforces its identification with the disturbed gas in the outflowing winds. Using only the *broad* component, we calculate the mass outflow rate ($\dot{M}_{out}$), finding values of up to $10\,M_{\odot}\,yr^{-1}$. The outflow kinetic power ($\dot{E}_{out}$) reaches maximum values between 10^{41} and $10^{43}\,erg\,s^{-1}$, which corresponds to feedback efficiencies of $\sim 0.001 - 0.1\,\%$ of L_{Bol}. These values are below those found in simulations and analytical models in order to quench star formation during the evolution of galaxies. However, our calculations consider only the contribution from the ionized gas to the outflow power, which represents only a fraction of the total power released by the feedback. We also investigated the relationship of $\dot{M}_{out}$ and $\dot{E}_{out}$ with L_{Bol}, and the effect of uncertainties on the values of some quantities – such as the electron density and the mass of the ionized gas in outflow – to the final values of $\dot{M}_{out}$ and $\dot{E}_{out}$.

Keywords: Active Galaxies. Quasars. Feedback. Emission Lines. Supermassive Black Holes.

Lista de ilustrações

Lista de tabelas

Sumário

1 Introdução

1.1 Núcleos Ativos de Galáxias

Galáxias são compostas por estrelas, poeira, gás e matéria escura. A presença, quantidade e distribuição desses ingredientes permitem a classificação das galáxias em diferentes tipos: espirais, elípticas, perturbadas, etc. Podendo também estar presentes, os Núcleos Ativos de Galáxias (AGN, de *Active Galactic Nuclei*) são regiões compactas que emitem radiação não estelar existentes no centro de algumas galáxias, descobertos entre as décadas de 1940 e 1960 (Seyfert, 1943; Schmidt, 1963). Outras características (Peterson, 1997) são:

- ◇ A região emissora da radiação do contínuo é muito compacta ($r \lesssim 1pc$), sendo que apenas recentemente observações dedicadas obtiveram sucesso em resolvê-la espacialmente (Event Horizon Telescope Collaboration et al., 2019). Para os objetos mais luminosos, essa radiação é mais intensa que o emitido pelo restante da galáxia.

- ◇ A radiação emitida pode possuir alta variabilidade de fluxo em vários comprimentos de onda. Flutuações observadas na ordem de dias sugerem escalas espaciais da ordem de $\sim 10^{-3}\,\mathrm{s}$.

- ◇ Linhas de emissão estreitas, cujas larguras nos perfis sugerem a origem em um gás perturbado, com velocidades de $10^2 - 10^4\,\mathrm{km\,s^{-1}}$. Em comparação, a velocidade orbital das estrelas no potencial da galáxia é da ordem de $\sim 10^2\,\mathrm{km\,s^{-1}}$. A baixa densidade eletrônica desse gás ($n_e \sim 10^2 - 10^5\,\mathrm{cm^{-3}}$) permite a observação de linhas proibidas, ausentes em regiões mais densas (onde seriam de-excitadas colisionalmente). Dizemos que essa radiação provém da Região de Linhas Estreitas (NLR, de *Narrow Line Region*).

- ◇ Alguns objetos possuem linhas de emissão alargadas, chegando a dispersões de velocidades de $\sim 10^4\,\mathrm{km\,s^{-1}}$. Com densidade elevada ($n_e \sim 10^8 - 10^{11}\,\mathrm{cm^{-3}}$), o gás emissor origina-se de regiões com raios típicos inferiores a 1 pc, chamadas de Regiões de Linhas Largas (BLR, de *Broad Line Region*).

- ◇ Jatos rádio, produzidos por partículas/íons viajando a velocidades relativísticas, provenientes do núcleo.

Esses fenômenos são consequências da acreção de matéria ao Buraco Negro Supermassivo (SMBH, de *SuperMassive Black Hole*) no centro das galáxias. A energia surge da conversão de energia gravitacional de matéria capturada pelo SMBH em radiação e energia cinética,

ocorrendo durante a acreção de gás até as regiões centrais. Durante esse processo, radiação pode ser liberada através de um disco de acreção, devido à sua viscosidade. A partir das bordas internas do disco também podem ser gerados jatos de partículas ionizadas resultantes de um campo magnético intenso local. Esse disco é circundado por um toro de poeira, que bloqueia parte da radiação oriunda do núcleo. A Figura 1 esquematiza a composição de um AGN no "modo radiativo" (mais detalhes abaixo).

A presença do toro de poeira causa uma restrição nas possíveis direções pelas quais os fótons podem escapar do AGN, resultando em uma assimetria na distribuição do gás por ele ionizado. Desta forma, conforme o ângulo de visada, não conseguimos observar a radiação emitida pelo disco de acreção e pela BLR. Isso leva a classifição de AGNs em: tipo I, onde observamos a BLR, pois nossa linha de visada em direção ao núcleo não é obstruída pelo toro; e tipo II, onde não detectamos a BLR, devido ao bloqueio pelo toro. Entretando, o toro não é uma estrutura contínua, mas sim um aglomerado de poeira e gás com 'buracos' por onde a radiação pode escapar (Nenkova et al., 2008; Ramos Almeida; Ricci, 2017; Audibert et al., 2017). Dessa forma, existe uma probabilidade não nula (Elitzur, 2012) de observamos um AGN tipo I, temporariamente como tipo II, e vice-versa.

A classificação em tipos I e II é a base do Modelo Unificado dos AGNs (Antonucci, 1993), a forma mais simples de tentar explicar diferentes classes de AGNs. Todavia, atualmente existem propostas mais elaboradas de modelos, que visam explicar uma gama maior de fenômenos. Netzer (2015) apresenta dois "modos de funcionamento":

- ◇ Modo radiativo (*radiative mode*): caracterizado por uma alta eficiência na conversão de energia gravitacional em radiação ($>1\%$). A acreção ocorre através do disco de acreção, circundado pelo toro de poeira – como descrito acima. Apesar de menos frequente, o jato em rádio (descrito no modo jato, abaixo) pode estar presente. Neste caso, dizemos que o AGN é *radio-loud*, e *radio-quiet*, caso contrário. Esse modo é frequentemente observado em galáxias com maior disponibilidade de gás frio (em geral galáxias espirais), que alimenta o SMBH e frequentemente também formação estelar em regiões circumnucleares.

- ◇ Modo jato (*jet mode*): possui baixa eficiência ($<1\%$) em relação ao modo radiativo. Neste modo, o gás (aquecido) chega ao SMBH, sem passar pelo disco fino. Um toroide de íons se forma, facilitando a produção de jatos de partículas relativísticas – que produzem os jatos em rádio. Este modo ocorre principalmente em galáxias massivas, em geral elípticas ou lenticulares, onde há pouco gás frio e pouca formação estelar.

Podemos também separar os AGNs em diversas categorias – principalmente por razões históricas – conforme propriedades específicas de cada grupo. Por exemplo, conforme a sua luminosidade, podemos dividir AGNs no modo radiação em: Seyferts, com luminosidades L_{AGN} abaixo de $\sim 10^{45}\,\mathrm{erg\,s^{-1}}$, e quasares, com luminosidades acima. Também

pode-se aumentar a classificação, conforme outras propriedades (e.g., razões de linhas de emissão e variabilidade temporal no fluxo), resultando em um número maior de categorias, como LINERs e Blazares. Em especial, neste trabalho analisaremos uma amostra de quasares de tipo II.

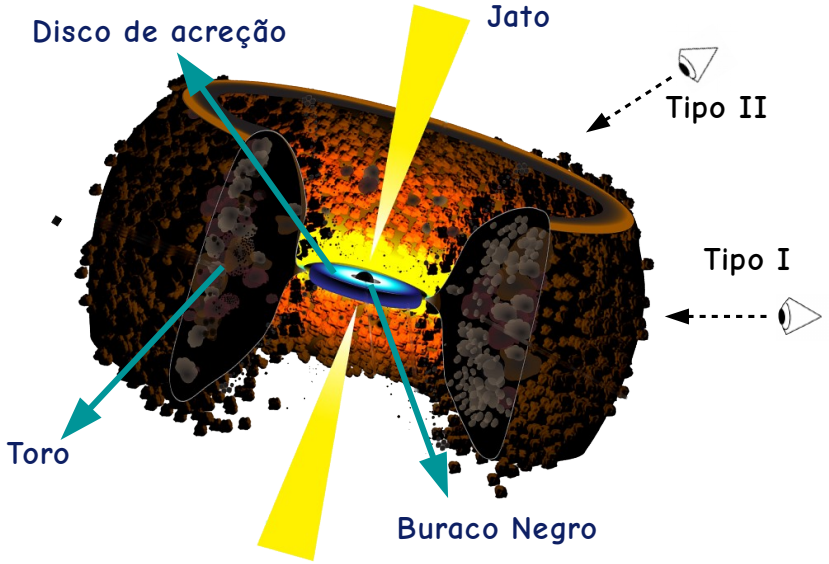

Figura 1 – Esquema da composição de um AGN no modo radiativo (imagem adaptada de B. Saxton NRAO/AUI/NSF). O disco de acreção de matéria (disco em azul) é circundado por um toro de poeira (nuvens marrons/laranja). Um jato de partículas (amarelo) também pode estar presente em alguns casos. A radiação da BLR tem origem em regiões próximas ao disco de acreção, enquanto a NLR surge mais externamente, chegando a ser observada a kpcs de distância do núcleo. Observando o AGN ao longo eixo de ionização, detectamos a radiação da BLR (AGN tipo I). No entanto, ao observá-lo de perfil (tipo II), a estrutura de poeira bloqueia a radiação nuclear. Os ângulos de visadas correspondentes estão destacados com setas vermelhas na figura.

1.2 Feedback

Nas últimas décadas, o número de estudos sobre o papel dos AGNs na evolução das galáxias cresceram consideravelmente (Heckman; Best, 2014; Fabian, 2012). No âmago do assunto estão os eventos de retro-alimentação (*feedback*) de AGNs, que agem sobre a galáxia hospedeira, podendo limitar o seu crescimento ao cessar (ou diminuir) a taxa formação estelar local. Essa regulação ocorre como consequência da energia liberada pelos núcleos ativos durante o processo de acreção (Storchi-Bergmann; Schnorr-Müller, 2019). Sua implementação em simulações hidrodinâmicas cosmológicas (e.g. Schaye et al. (2015), Nelson et al. (2019)) e modelos semi-analíticos (e.g., Croton et al. (2016), Gonzalez-Perez et al. (2014)) é necessária para a reprodução de propriedades observadas no Universo, como a frequência de galáxias massivas no Universo local, que é menor do que a previsão de modelos sem *feedback* (Silk; Mamon, 2012). No entanto, diferentes implementações são capazes de reproduzir essa e outras propriedades (Somerville; Davé, 2015). Assim, é

preciso saber como o *feedback* de AGNs atua e qual o seu grau de influência na evolução de galáxias em comparação com outros fenômenos, como colisões entre galáxias (*mergers*) e explosões de supernovas (Man; Belli, 2018).

Algumas correlações entre propriedades dos AGNs e suas galáxias hospedeiras estão entre os fatores seguidamente citados como evidência de *feedback* de AGNs. Entre as mais conhecidas, estão a relação entre a massa do SMBH e a dispersão de velocidades estelar em bojos clássicos (Ferrarese; Merritt, 2000, $M_{BH} - \sigma_*$) e com a massa estelar dos mesmos (Marconi; Hunt, 2003, $M_{BH} - M_*$). No modo jato, existem evidências diretas de *feedback* (e.g. Ciotti, Ostriker e Proga (2010)), onde íons/partículas relativísticos depositam energia no meio interestelar/galático. Neste caso, o gás aquecido não colapsa num disco, desfavorecendo a formação estelar. Contudo, AGNs com *feedback* intenso neste modo são raros (Heckman; Best, 2014), o que indica que outros processos de regulação também podem ser importantes. Por outro lado, AGNs no modo radiação são mais abundantes. Neste caso, a radiação produzida no disco de acreção transfere energia e momentum para o gás, podendo gerar um fluxo de matéria para regiões mais externas (*outflows*). Esses *outflows* são observados diretamente no Universo local (e.g. Schnorr-Müller et al. (2014), Lena et al. (2015)). Para esses AGNs, que são menos luminosos, os *outflows* possuem extensões $\lesssim 1\,\mathrm{kpc}$, pequenas em comparação com a escala de tamanho das galáxias ($\sim 10 - 10^2\,\mathrm{kpc}$). Entretanto, para AGNs mais luminosos (QSOs), existem evidências de *outflows* com extensões $\gtrsim 10\,\mathrm{kpc}$ (Liu et al., 2013).

Para investigar e quantificar a influência do *feedback* no modo radiativo, é necessário estudar as propriedades dos *outflows* – como suas extensões e energias liberadas – em AGNs com diferentes luminosidades. Isto pode ser estimado através de fotometria de alta resolução espacial (Bennert et al., 2002; Schmitt et al., 2003a). Em particular, nosso estudo anterior (Storchi-Bergmann et al., 2018) apresentou uma correlação entre a extensão da região ionizada pelo AGN e a sua luminosidade, atingindo $\sim 20\,\mathrm{kpc}$ para luminosidades bolométricas de $\sim 10^{47}\,\mathrm{erg\,s^{-1}}$. No entanto, a ausência de informação espectral resolvida impede a determinação de qual a porcentagem desse gás ionizado realmente está em *outflow*. Uma técnica de análise adequada para isto é a utilização de Espectroscopia de Campo Integral (IFS, de *Integral Field Spectrocopy*), que permite explorar a informação espacial e espectral de AGNs em um único cubo de dados. Vários estudos utilizam esta estratégia para estudar o gás em *outflow* (e.g. Harrison et al. (2014), Karouzos, Woo e Bae (2016), Husemann et al. (2016)). Esses estudos começaram a desvendar o impacto dos AGN's nas suas galáxias hospedeiras, revelando a presença de *outflow* não apenas em gás ionizado mas também em outras fases como a molecular e atômica (e.g. Feruglio et al. (2015)). Entretanto, devido a diferentes métodos de cálculos das propriedades de interesse, como taxas de ejeção de massa e potência do *outflow*, os valores obtidos por autores distintos para objetos semelhantes podem variar bastante (Harrison et al., 2018).

Tentando normalizar as estimativas, Fiore et al. (2017) compilaram dados da literatura com cálculos para o gás em diferentes fases (ionizado, molecular e em raio-X). Esses autores encontraram correlações positivas entre a luminosidade do AGN e as taxas de ejeção de massa e potência do *outflow*. Isso indica que AGNs mais luminosos podem ser suficientemente poderosos a ponto de ejetar quantidades consideráveis de matéria da galáxia, assim influenciando a sua evolução. No entanto, os cálculos exigiram diversas hipóteses simplificadas, de modo a permitir a sua aplicação a diferentes dados da literatura. Desta forma, também é importante realizar computações mais precisas, para verificarmos se as hipóteses utilizadas em diversos estudos são satisfatórias.

1.3 Objetivos

Este trabalho é um desdobramento de nosso estudo anterior (Storchi-Bergmann et al., 2018), onde analisamos uma amostra de nove quasares tipo II – com luminosidades entre $10^{45} < L_{Bol} < 10^{47}\,\mathrm{erg\,s^{-1}}$ e redshifits $0.1 < z < 0.5$, utilizando imageamento em bandas estreitas, centradas nas linhas de emissão [O III]λ5007 e Hα, obtidas com o Telescópio Espacial Hubble. Foram estudados AGNs tipo II, pois o espectro possui uma contribuição pequena (ou nula) da BLR, facilitando o estudo do gás proveniente da NLR. Essa faixa de luminosidades, por sua vez, permite analisar objetos mais luminososos em comparação com estudos similares anteriores (Schmitt et al., 2003b; Bennert et al., 2002). Como resultado, encontramos regiões vastas de gás ionizado pelos AGNs (ENLR), com raios de até 18 kpc, como é o caso de J135251, como ilustrado na Figura 2. A ENLR estendia-se além da região ocupada pelas estrelas da galáxia hospedeira, caso houvesse gás disponível nesses locais, que nestes casos ocorria principalmente por eventos recentes de *mergers*.

No entanto, embora a radiação proveniente do disco de acreção possua grande alcance – o que poderia representar indícios de um *feedback* intenso – não é possível afirmar qual a porcentagem do gás ionizado está realmente em *outflow*. Para tanto, é vital obter dados que nos permitam estudar a cinemática do mesmo.

Nossos objetivos neste trabalho foram:

- Obter dados de Espectroscopia de Campo Integral (IFS, *Integral Field Spectroscopy*) para poder obter, de forma espacialmente resolvida, parâmetros das linhas de emissão;
- A partir das intensidades das linhas de emissão, obter as massas de gás correspondentes;
- Com a cinemática, obtida a partir dos perfis das linhas, combinadas com a massa do gás ionizado, obter a taxa de ejeção de massa e a potência do *outflow*;

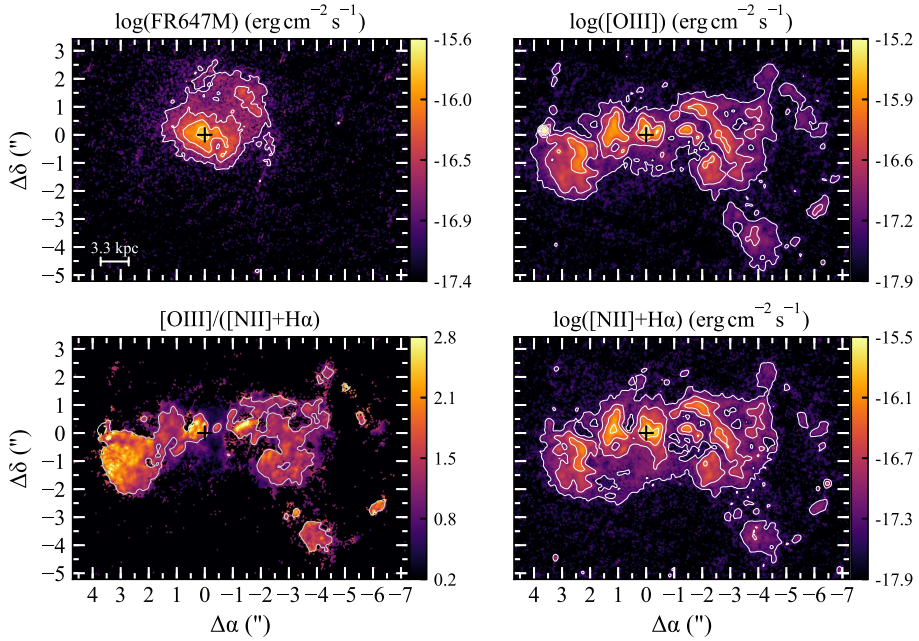

Figura 2 – J135251.21+654113.2. Imagens em bandas estreitas do HST, centradas no contínuo estelar (topo, à esquerda), [O III] (topo, à direita) e [N II]+Hα (embaixo, à direita). O mapa de excitação (embaixo, à esquerda), obtido da razão [O III]/([N II]+Hα), traça a fonte de ionização: valores mais elevados (dentro do contorno) representam regiões ionizadas pelo quasar. Esse gás se estende por até $\sim$17 kpc em raio, para além da região do contínuo estelar ($\sim$5 kpc).

- Comparar a potência do *outflow* com a luminosidade do AGN para verificar se esta potência atinge valores de 0.5–5%, que indicam se *outflow* é poderoso o suficiente para impactar a evolução da galáxia hospedeira, segundo simulações e modelos analíticos.

- Comparar com resultados prévios da literatura para AGNs de luminosidade semelhante, e avaliar a influência dos diferentes métodos de cálculo nas taxas de ejeção de massa e potência obtidas.

Desta forma, observamos parte da nossa amostra – oito QSOs tipo II – com o instrumento GMOS-IFU (*Gemini Multi-Object Spectrographs – Integral Field Unit*) dos Telescópios Gemini (Norte e Sul). Após modelarmos os perfis das linhas de emissão observadas, calculamos grandezas relacionadas as propriedades dos *outflows*. Com as intensidades obtidas, comparamos nossos resultados com dados da literatura, de modo a verificar a influência dos diferentes métodos de cálculo e de suas incertezas nos valores obtidos e assim identificar o possível impacto destes quasares na evolução da galáxia hospedeira.

Nos Capítulos 2 e 3 detalhamos a nossa amostra e o processo de redução de dados, enquanto que nos Capítulos 4, 5 e 6, apresentamos as metodologias e os resultados, acompanhados de uma discussão sobre os mesmos. Estes capítulos, de 2 a 6, estão redigidos em Inglês pois fazem parte de um artigo científico que será submetido em breve para

publicação. Por fim, no Capítulo 7 apresentamos nossas conclusões, redigidas em Português, assim como a Introdução.

2 Sample

Our sample consists of 7 type II QSOs from our original 9 objects (Storchi-Bergmann et al., 2018), which were drawn from the Reyes et al. (2008) sample. They were originally selected for having luminosities $L_{[O\,III]\lambda5007}$ above 10^{42}erg s^{-1}, and redshifts in the range $0.1 < z < 0.5$: luminous objects that could still be resolved by HST imaging observations. We added 1 similar object (J120041) from Fischer et al. (2018), to enable the total usage of the acquired observation time of the proposal, since its sky position were less disputed by other observers in comparison with the originally proposed object. Incidentally, most of these galaxies have signs of mergers (see discussion in Storchi-Bergmann et al. (2018)), as seen in the HST continuum maps (Fig. 3), which agrees with previous findings that a high incidence of mergers is correlated with strong nuclear activity (e.g. Treister et al. (2012)), using $L_{[O\,III]}$ as a proxy for L_{Bol}.

Some basic information of the sample objects is presented in Table 1, that contains their short name identifications (full name in Table 2), systemic redshifts (z, see 4.4), [O III]λ5007 luminosity, angular scales and luminosity distances (D_L). We also identify, in the last column, the work from which the objects were drawn. The angular scale was used to convert spatial distances from arcsec to kpc, and D_L to obtain luminosities from fluxes. These two quantities were derived from the redshift, using the cosmological calculator of Wright (2006), after the redshfits were corrected for the CMB dipole model (Fixsen et al., 1996).

Tabela 1 – Sample

Name	z	$L_{[O\,III]}$	Scale	D_L	Ref
(1)	(2)	(3)	(4)	(5)	(6)
J082313	0.4331739	25.0	5.46	2310	a
J084135	0.1107256	5.4	1.95	498	a
J085829	0.4539375	11.6	5.61	2450	a
J094521	0.1284013	6.47	2.22	583	a
J123006	0.4070136	21.8	5.26	2149	a
J135251	0.2065747	18.8	3.26	980	a
J155019	0.1429503	4.83	2.42	653	a
J120041	0.1158399	8.33	2.04	524	b

(1) galaxy short name (full name in Table 2); (2) redshift; (3) [O III]λ5007 luminosity (in units of 10^{42} erg s^{-1}); (4) spatial scale (in kpc/arcsec); (5) luminosity distance (in Mpc); (6) original sample: (a) Storchi-Bergmann et al. (2018), (b) Fischer et al. (2018).

3 Observations and data reduction

3.1 Observations

Observations were undertaken with the Integral Field Unit (IFU, Allington-Smith et al. (2002)) of the Gemini Multi-Object Spectrographs (GMOS) available in both Gemini telescopes. The details of the observations are displayed in Table 2. The GMOS-IFU field-of-views are shown as green rectangles over HST narrow images in Fig. 3, and the spectra of the sample – integrated over a 2 kpc radius aperture in the IFU data cubes – are displayed in Fig. 4.

The instrument offers two configurations. The one slit mode (identified as IFU-R in the table) with 500 fibers covering a field-of-view of $5'' \times 3.5''$, and other 250 dedicated to the sky. The other mode – two slit (IFU-2) – has 1000 fibers covering $5'' \times 7''$, with other 500 for the sky, and a smaller wavelength range. For our observations, we opted for the one-slit mode because it enables the observation of more emission lines: Hβ, [O III]$\lambda\lambda$4959,5007, Hα, [N II]$\lambda\lambda$6548,84 and the pair [S II] $\lambda\lambda$6718,31. In order to cover these lines and still have an adequate spectral resolution, R400 and B600 gratings were the best choices. When necessary, filters were used to block second-order contamination of the spectra. For each object, several expositions were performed, aiming to: achieve a signal-to-noise ratio (S/N) above 3 at mid distances between the nucleus and regions at the borders of the IFU FoV; fill the spectral gaps (caused by the gaps between the CCDs) and the spatial holes (caused by dead lenslets/fibers), by means of dithering (offsetting) the observations in the spectral and spatial dimensions, respectively. The total exposure of the combined observations is also shown in the table, along with the reference of the published results of the data collected from Gemini Archive.

The archival data – used for J085829 and J094521 – does not match all the above requirements of our own observations (see Fig. 4). J085829 observations used the two-slit mode (IFU-2), resulting in a much smaller wavelength range, covering only Hβ and [O III]. In the case of J094521, the use of the B1200 grating, which has a higher resolution, and consequently smaller spectral coverage, also results in a spectrum with only these three emission lines.

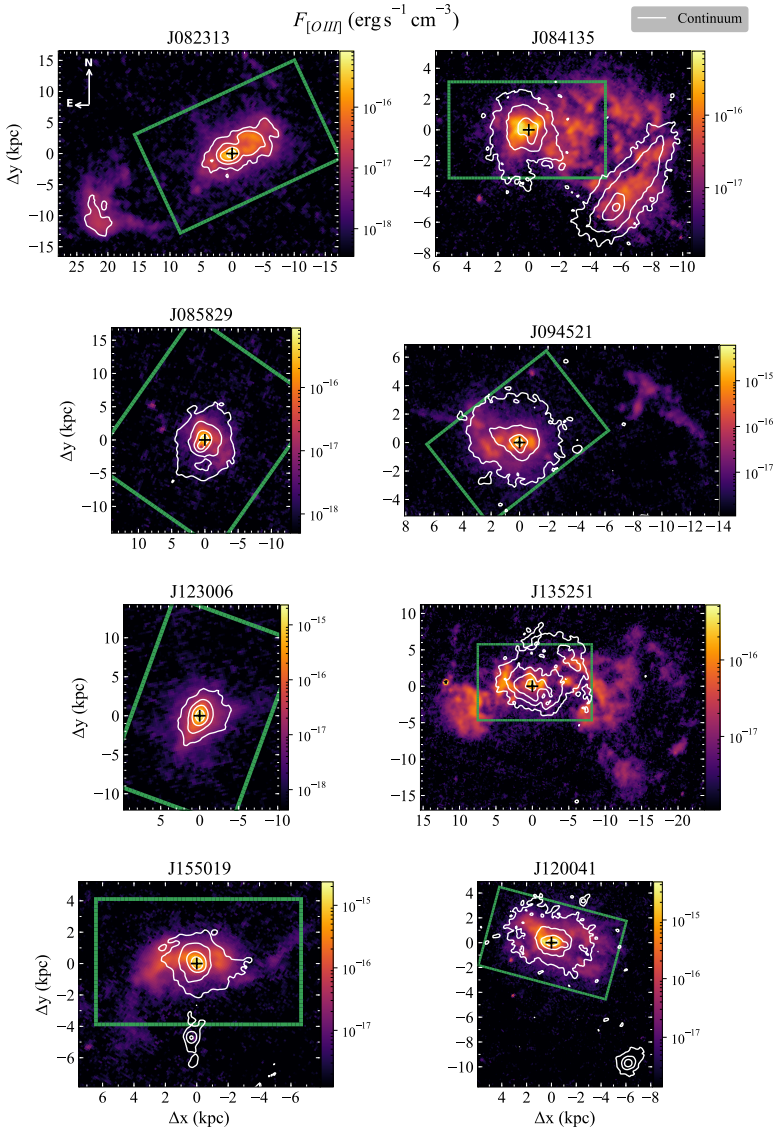

Figura 3 – HST narrow-band images of our sample. The colormaps are tracing the [O III]flux distribution of the galaxies, with its continuum superposed as white contours. The GMOS-IFU field-of-views are highlighted as green rectangles.

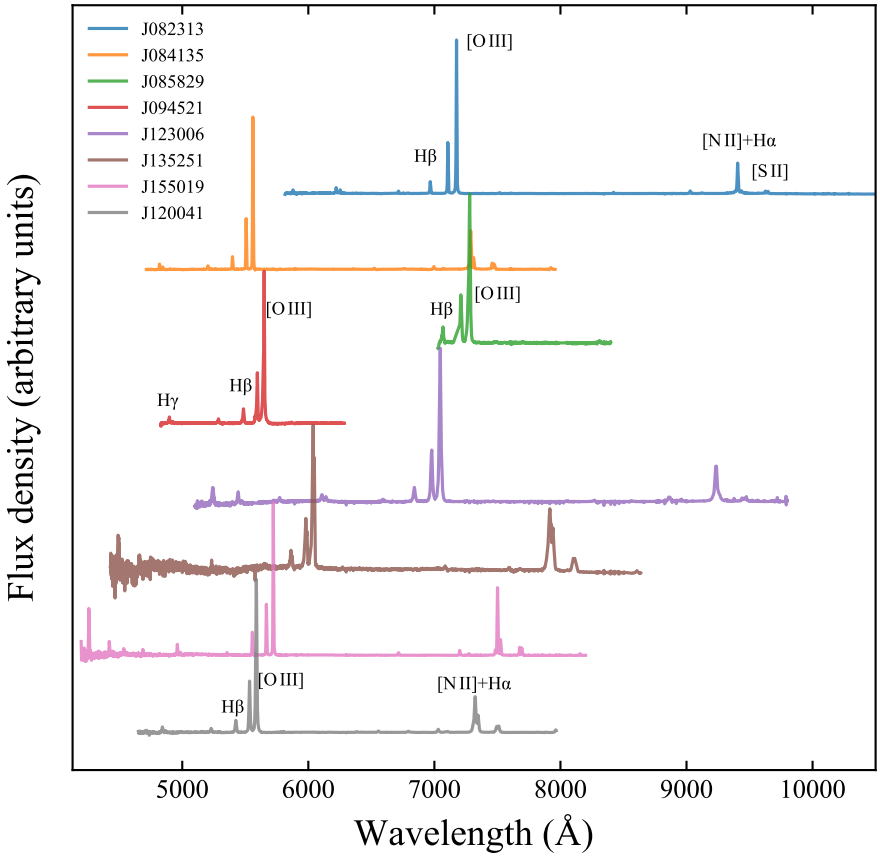

Figura 4 – Spectra of the galaxies of our sample, integrated over a 2 kpc radius aperture in the data cube. Not corrected for redshift.

Tabela 2 – Observations

Name (1)	Full name (2)	Observation ID (3)	Grating (4)	Filter (5)	Mode (6)	Exptime (7)	Ref (8)
J082313	SDSS J082313.50+313203.7	GN-2018B-Q-207	R400_G5305	GG455_G0305	IFU-R	6240	-
J084135	SDSS J084135.04+010156.3	GS-2018B-Q-110	B600_G5323	open	IFU-R	8920	-
J085829	SDSS J085829.58+441734.7	GN-2010B-C-10	R400_G5305	i_G0302	IFU-2	3600	c
J094521	SDSS J094521.34+173753.3	GS-2010A-Q-8	B1200_G5321	open	IFU-R	5202	d
J123006	SDSS J123006.79+394319.3	GN-2019A-Q-228	R400_G5305	GG455_G0305	IFU-R	4800	-
J135251	SDSS J135251.21+654113.2	GN-2019A-Q-228	R400_G5305	open	IFU-R	3450	-
J155019	SDSS J155019.95+243238.7	GN-2018A-Q-206	R400_G5305	open	IFU-R	5400	-
J120041	FIRST J120041.4+314745	GN-2019A-Q-228	B600_G5307	open	IFU-R	3735	-

(1) and (2) galaxy short and full name; (3) Gemini observation ID; (4) and (5): gratings and filters full names; (6) IFU-R is one-slit and IFU-2 is two-slit mode; (7) total exposure time (in seconds); (8) references of the published results, when the IFU data were taken from Gemini Archive: (c) Liu et al. (2013), (d) Harrison et al. (2014).

3.2 Data reduction

The IFS data reduction was carried out with the Python package `GIREDS`[1]. This software automatizes the process, applying the recommended steps – which include the reduction of both the standard star and the science files – using the `IRAF`'s (Tody, 1986) packages provided by Gemini. However, some steps had to be done interactively. The wavelength calibration – performed by the `GSWAVELENGTH` task – failed to find a solution for some objects, in which cases we did it interactively. We also opted to execute the flux calibration of all objects interactively, using the standard task `GSSTANDARD`, which improved the automatic solution. After the calibration, the software creates a data cube file for each science observation of each galaxy. We over-sampled the final pixel scale: instead of using the diameter of the fibers ($\sim 0.2''$), we choose a scale of $0.1''$/pixel. During the last step, the data were corrected for differential atmospheric refraction.

At this step, each galaxy has a set of data cubes spatially offsetted from each other. Using the instrumental offsets (listed in the header), we combined all observations into a final data cube, containing the calibrated flux and its uncertainties (propagated from the Poission statistics of the uncalibrated data).

3.3 Complementary data

Along with the integral field spectroscopy data, we made use of the available HST data from Storchi-Bergmann et al. (2018). It consists of narrow-band images centered on [O III] and Hα emission lines, and in the continuum between these two lines (used to subtract its contribution from the emission line images). We also used the analogous HST [O III] data of J120041 from Fischer et al. (2018). The applied data reduction procedure is described in Storchi-Bergmann et al. (2018).

[1] <https://bitbucket.org/danielrd6/gireds>

4 Methodology

4.1 Emission line fitting

In order to retrieve the ionized gas kinematic and excitation information, we proceeded to model the emission lines with multiple Gaussian function. A Gaussian profile is characterized by three parameters: the radial velocity (v) that corresponds to the bulk of motion of the gas clouds in a given position in the sky; the velocity dispersion (σ), where higher values usually can be associate with a more disturbed gas; and the amplitude (A), that along with the other two parameters enables us to calculate the total flux (F) of the line. When using multiple Gaussian profiles to fit an emission line, we are considering that each component is measuring the properties of a group of clouds along the line-of-sight in that pixel. In our fits, we used up to four Gaussians to model each emission line, with the same number of components for all pixels of a given object.

Considering that outflows disturb the gas kinematically, we assumed that one of the components is modelling this disturbance: the *broad* component. To implement this, we impose that, for a given pixel, this component always has a larger σ. The remaining components are called *narrows* (e.g. *narrow* 1) and, in principle, are originated in clouds that are not in outflow. However, in our sample, the majority of the galaxies have signs of interactions: HST continuum images (see contours in Fig 3) show a perturbed distribution of the continuum flux, and in some cases, the presence of an interaction companion. Hence, the *narrow* components are not only modelling the less disturbed gas in the disk of the galaxy, but also the gas from the different objects involved in the interaction, with initial non-zero relative velocities. Because of this, we needed to use more than one narrow component in almost all of our galaxies, because there were regions where we couldn't model it using only one *narrow* and one *broad* component (see Fig. 5).

When present, we fitted simultaneously the following emission lines, using the same number of *narrow* and *broad* components for each one: Hβ, [O III]$\lambda\lambda$4959,5007, Hα, [N II]$\lambda\lambda$6548,84 and [S II]$\lambda\lambda$6718,631. We force the *narrow* and *broad* components to have the same kinematic properties for all emission lines: v and σ (in units of km s^{-1}) of the *broad* components of all lines is the equal, and equivalently for each one of the *narrow* components, individually. Some objects have signal-to-noise ratios (S/N) high enough in other emission lines (e.g. [O III]λ4362 and Hγ) that can help to constrain the properties of the gas. We fitted these lines with a maximum of two Gaussians (without distinguishing it in *narrow* or *broad*) because we are only interested in its total flux (summed between components) and its lower S/N does not enable the clear separation into more components.

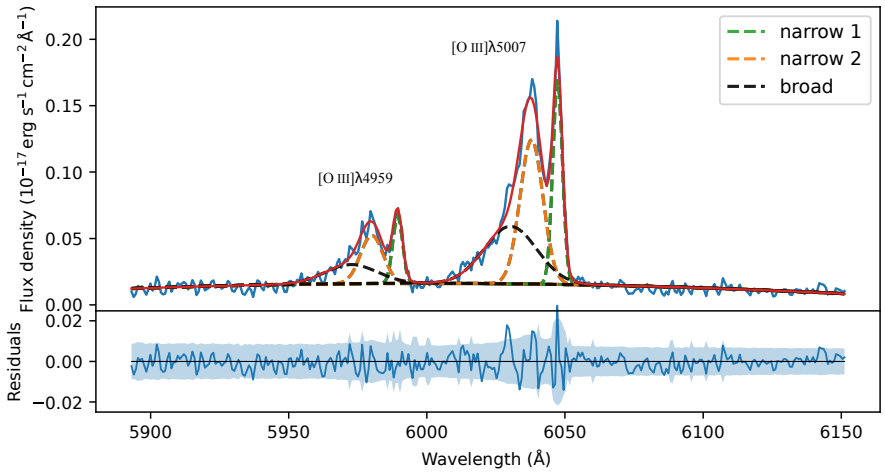

Figura 5 – Fitting result of one spectrum from J135251 in the region of [O III]emission lines. Three components were needed: 2 *narrows* and 1 *broad*.

To decrease the number of fitting parameters, we fixed the ratios between emission flux lines (Osterbrock; Ferland, 2006, approximated from Table. 3.12): [O III]$\lambda\lambda$5007/4959 = 3 and [N II]$\lambda\lambda$6584/6548 = 3. We also added the following flux constraints, to avoid non-physical solutions: Hα/Hβ > 2.74 (intrinsic recombination value for $T_e = 2{\times}10^4$ K and $n_e = 10^2\,\mathrm{cm}^{-3}$, as displayed in Table 4.4 in the above reference); and 0.436 < [*S II*]$\lambda\lambda$6718/6731 < 1.496 (Proxauf; Öttl; Kimeswenger, 2014, asymptotic values for high and low densities). Each one of these bounds/constraints was applied to each component (e.g. *narrow* 1) individually.

The fitting procedure was performed using the software `IFSCUBE`[1]. This program uses `SCIPY` implementations of non-linear minimization and permits the addition of constraints and bounds to the parameters. Initially, a guess to the parameters of an initial pixel – one of the brightest ones – is given. Then, the program fits the rest of the pixels, updating the initial guess based on the successful fits of the neighbour spectra. First, this procedure was done only for the [O III]$\lambda\lambda$4959,5007 emission lines, because of their high S/N. After we became satisfied with the initial guess and the number of components needed, we repeated the fitting process for all lines of interest. An example of a fit is shown in Fig 5, where we can see that we needed to deblend each emission line into three components: *narrow* 1 ($n1$), *narrow* 2 ($n2$) and *broad* (b). More examples of fits are displayed in Fig 11–18, showing the complexity of the emission line profiles.

4.2 Gas temperature, density and reddening

It would be ideal to obtain the electron density and the reddening for the *broad* and *narrow* components individually. However, the poor S/N of the *broad* component of

[1] <https://github.com/danielrd6/ifscube>

the emission lines involved in the calculations (Hα, Hβ and [S II]) makes it not suitable to obtain these parameters over a large extent. Therefore, we used the sum of its fluxes (e.g. $F_{\mathrm{H}\alpha} = F_{\mathrm{H}\alpha,b} + F_{\mathrm{H}\alpha,n1} + ..$) to obtain these properties with the equations below.

Nebular line diagnostic is an important tool used in Astronomy to constrain the properties of the gas in galaxies. As an example, the ratio between the pair of lines [S II]$\lambda\lambda$6718,31 gives a measure of the electron density (n_e). Therefore, assuming the typical NLR electron temperature in AGNs of $T_{\mathrm{e}} = 10^4 K$, we obtained n_e with the formula from Proxauf, Öttl e Kimeswenger (2014).

To measure the extinction caused by the dust in the galaxies, we compared the observed ratio of hydrogen Balmer emission lines with its intrinsic recombination value for a given electron temperature and density. The color excess $E(B-V)$ is given by Revalski et al. (2018):

$$E(B-V) = \frac{2.5 \log\left(\frac{(\mathrm{H}\alpha/\mathrm{H}\beta)_i}{(\mathrm{H}\alpha/\mathrm{H}\beta)_o}\right)}{R_{\mathrm{H}\alpha} - R_{\mathrm{H}\beta}}, \tag{4.1}$$

where the reddening values $R_{\mathrm{H}\alpha}$ and $R_{\mathrm{H}\beta}$ are from Savage e Mathis (1979). The intrinsic recombination values $(\mathrm{H}\alpha/\mathrm{H}\beta)_i$ are from Osterbrock e Ferland (2006) (case B, in their Table 4.4), where we interpolated between the values of the tables, to match the density and temperature in the pixel. To correct the flux from a given emission line, we used (Revalski et al., 2018):

$$F_{x,i} = F_{x,o} \cdot 10 \cdot \exp\left[0.4 \cdot E(B-V) \cdot (R_x - R_{\mathrm{H}\beta})\right], \tag{4.2}$$

with $F_{x,o}$ and $F_{x,i}$ being the observed and the corrected (in relation to Hβ) flux of a given emission line (x), while R_x is the reddening value at the wavelength of the line being corrected for extinction. For J094521, we used the ratio Hβ/$H\gamma$, because its spectra do not cover the Hαregion (see Fig. 4). We don't apply an extinction correction for J085829, since its spectrum only covers one Balmer line.

4.3 Ionized gas mass

The mass of the ionized gas ($M_{\mathrm{H\,II}}$) can be obtained from the luminosity of H II emission lines. We choose to use Hα, since it has the highest S/N and hence covers the largest spatial extent. However, we used Hβ for J085829 and J094521, since their spectra do not cover this emission line (see Fig. 4). Ignoring the small contribution from ions other than H II to the total gas mass, we can use the formula (Storchi-Bergmann et al., 2018):

$$M_{\mathrm{H\,II}} = \frac{m_p\, L(H\beta)}{n_e\, \alpha^{eff}_{H\beta}\, (h\,\nu_{H\beta})}, \tag{4.3}$$

where m_p is the proton mass, $L(H\beta)$ is the Hβluminosity (calculated from its flux and D_L from Table 1), $h\,\nu_{H\beta}$ is the energy of the transition, $\alpha^{eff}_{H\beta}$ is the effective recombination

coefficient of $H\beta$, and n_e is the electron density. Using the intrinsic emissivities ratio $j_{H\alpha}/j_{H\beta}$, we can convert Hα into Hβ luminosity, when it was the case. This ratio was obtained from Osterbrock e Ferland (2006), interpolating between the values of their Table 4.4, to match the particular electron temperature and density derived from each spectrum.

4.4 Outflow velocity

We made the hypothesis that the *broad* component is modelling the outflow. Therefore, following Rupke e Veilleux (2013) and Fiore et al. (2017), we define the outflow velocity (v_{out}) as:

$$v_{out} = |v_b - 2\,\sigma_b|\,, \tag{4.4}$$

where v_b is the centroid velocity (velocity shift relative to the galaxy systemic velocity) of the *broad* component, and σ_b its velocity dispersion. In this equation, we are signing a value of velocity at the blue side of the *broad* component as representative of the outflow velocity.

For two galaxies (J085829 and J135251), the systemic velocity was determined from the [Na I D] absorption lines: median velocity of $v_{[\mathrm{Na\,I\,D}]}$ over the field-of-view. In other cases, for which the [Na I D] absorption lines had a poor S/N ratio, it was adopted as the median velocity of the *narrow* component having a clearer rotation pattern.

The fitting process imposed that all *broad* components of a given spectrum have the same kinematics, hence we could use any emission line to calculate v_{out}. Therefore, we choose [O III]λ5007, since its higher S/N ratio (in relation to the other lines) allows its measurement up to larger distances from the nucleus.

4.5 Outflow properties

In order to trace the outflow, we are interested in the corresponding mass outflow rate ($\dot{M}_{out}$) and the outflow power ($\dot{E}_{out}$). Following Shimizu et al. (2019), we define:

$$\dot{M}_{out}(r) = \frac{M_{\mathrm{H\,II}}(r)\,v_{out}(r)}{\delta r}, \tag{4.5}$$

$$\dot{E}_{out}(r) = \frac{1}{2}\dot{M}_{out}(r)\,v^2_{out}(r), \tag{4.6}$$

where δr is the width of an annular aperture, at a given radius (r) with origin in the nucleus. The position of the nucleus was adopted to correspond to the peak of the continuum emission, while δr equals the size of 2 pixels (the cube has 0.1″/pix, and its scale is displayed in Table 1). We integrated $M_{\mathrm{H\,II}}(r)$ over all pixels inside the annulus, and the $v_{out}(r)$ is the average value inside the region.The $M_{\mathrm{H\,II}}$ of Eq. 4.5 was calculated using

$L(H\alpha)$ from the *broad* component, since we consider that it corresponds to the ouflowing gas.

The use of the above equations 4.5 and 4.6 imply that we are observing the velocity of the outflow component crossing each radius r, but we are actually measuring only the line-of-sight component of the velocity, that ideally should corrected for projection effects.

4.6 Signal-to-noise ratio

The value of the noise (N) has been adopted as the standard deviation in the continuum close to each emission line. For each component, we only used pixels in which the peak flux (S) emission has S/N $>$ 3. Although this makes us discard some data and therefore limit the extent of the components measurements, it also leads to an increase in the confidence of the remaining data. However, each emission line has different S/N and consequently covers a different extent. For example, there are regions in which [O III]λ5007 is strong, but the density cannot be determined. In such cases, we have used the median density values of the good S/N neighboring pixels to cover the regions that have no data. The reason for this is that we need n_e and $v_{[O\,III]}$ to obtain $\dot{M}_{out}$, and we want to use the maximum number of pixels in the calculation.

5 Results

5.1 Emission-line fitting

In Figs. 5 and 19–24, we present some examples of the results of the fitting process applied to the emission-lines of each galaxy, with the Gaussian profiles superimposed on the original spectra. Different rows correspond to different positions (pixels) in the field-of-view, with the columns being a zoom-in in the emission lines of Hβ, [O III], [N II], Hα and [S II]. We choose to show pixels with different characteristics, highlighting the fact that the number of components needed to model the emission lines may vary inside the field-of-view. We can also observe that the need of more than one *narrow* component is visible in different emission lines – e.g., the presence of double peaks in the profiles. This increases our confidence that the number of components used was indeed required.

5.1.1 Broad Line Region (BLR)

Even though our sample consists of QSOs classified as type II (Reyes et al., 2008), one of them – J082313 – showed signs of a weak BLR contribution (only visible in the Hαprofile). To model it, we first integrated the spectrum over a $1''$ aperture, covering the the region where there were spectra with signs of BLR emission. Then, we applied the fitting process (Section 4.1) to this integrated spectrum, using 1 *broad* and 3 *narrow* components to model the NLR gas, along with a broader Gaussian representing the BLR. The best fit result has $v_{BLR} = -150\,\mathrm{km\,s^{-1}}$ and $\sigma_{BLR} = 1270\,\mathrm{km\,s^{-1}}$. After determining the profile parameters for the BLR component, in order to reproduce the smearing effect of the atmospheric seeing on this componen, we fixed the v_{BLR} and σ_{BLR} at the above values, letting the amplitude be the only free paramenter of the BLR component. In Fig 11, it is possible to see the weak contribution the BLR in some of the fitting results. Using `ASTROPY`'s `modeling` module, we fitted a two-dimensional Gaussian over its flux distribution (Fig. 6), resulting in a FWHM of $\sim 0.57''$, corresponding to the seeing.

5.2 Maps

In this section, we present the result of the fitting process as maps of the model parameters. The maps are displayed in Fig. 7, and Figs. 19–25 in the Appendix A.2. In the first row, from left to right, we show maps of the galaxy continuum flux, the gas reddening, and the electron density maps, obtained from the integrated profiles. The other rows below display maps of the parameters of each component of [O III]λ5007: the left column

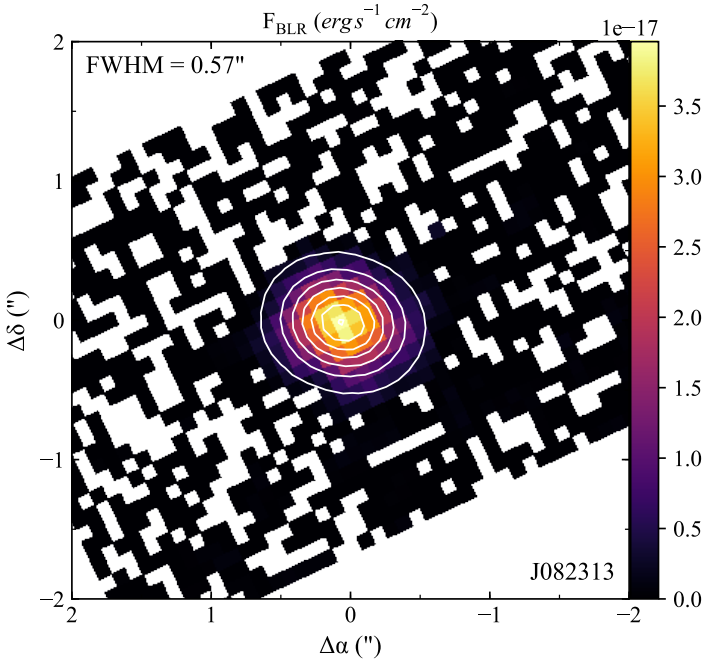

Figura 6 – HαBroad line region flux distribution of J082313, along with the 2D Gaussian fit (white contours). North is up and East is to left.

accounts for the flux of each component; the central, its radial velocity, and the right column shows its velocity dispersion. The last row refers to the *broad* component, that is adopted as being due to the outflow. The remaining middle rows refer to the *narrow* components. We choose to show the maps for [O III]λ5007 because it has the highest S/N, but the kinematics of the other emission lines are the same – as imposed by the fitting procedure (Section 4.1).

5.3 Radial profiles of $\dot{M}_{out}$ and $\dot{E}_{out}$

Using Eqs. 4.5 and 4.6, we obtained radial profiles of $\dot{M}_{out}$ and $\dot{E}_{out}$ from the *broad* component of the galaxies of our sample, by calculating medium values for these properties along each ring and plotting then as a function of the medium radius, as displayed in Fig. 8. In these profiles, we have used only the luminosity of the *broad* component of Hβ ($L_{\mathrm{H}\beta}$) to calculate $M_{\mathrm{H\,II}}$, in order to only include the contribution of the mass in outflow.

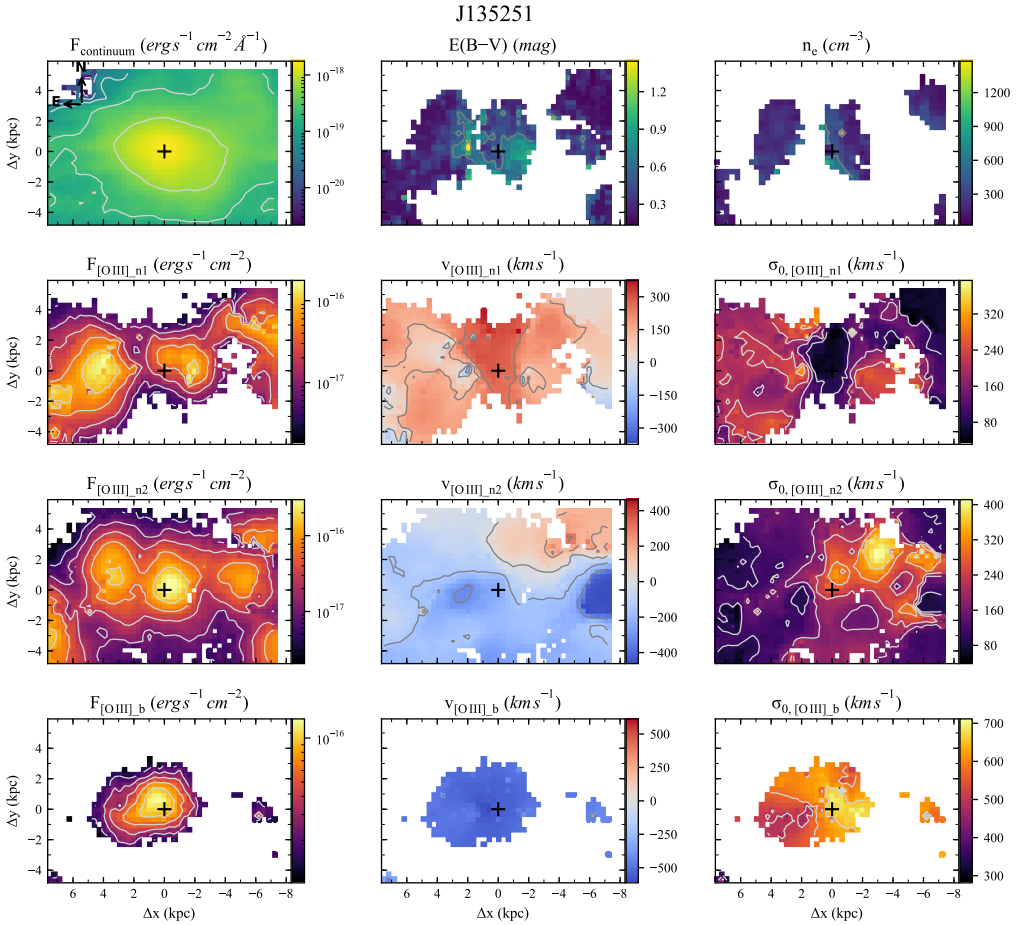

Figura 7 – Maps of J135251, result of the fitting process. In the first row, we show the continuum map around rest wavelength λ5600Å, the gas reddening, and the electron density maps. The remaining rows display the parameters of each component of [O III]λ5007: the left column accounts for the flux of each component; the center column, for the radial velocity; and the right column, the velocity dispersion. The second and the third rows refer to the two *narrow* components, while the last one refers to the *broad* component.

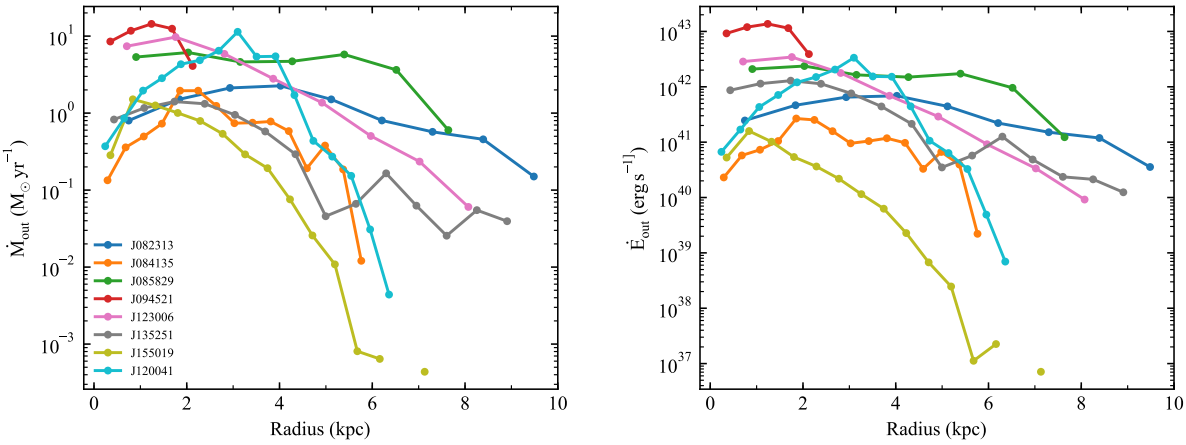

Figura 8 – Radial profile of $\dot{M}_{out}$ (left) and $\dot{E}_{out}$ (right) for the objects of our sample.

6 Discussion

6.1 Maps

The maps, presented in Fig. 7 and Figs. 19–25 in the Appendix A.2, display diverse and complex scenarios for the flux distributions and kinematics of the ionized gas in our sample galaxies. Besides the *broad* component, 5 QSOs needed more than one *narrow* Gaussian in order to model its emission line profiles (see Section 4.1). This could be a consequence of the high incidence of mergers in our objects: from Storchi-Bergmann et al. (2018, see Table 1) sample, only J082313 and J123006 do not show clear signs of interaction in the HST continuum map (see Fig. 3 and the discussion in the original paper). In the case of J085829, the only signature of an interaction seems to be a second continuum peak, close to the nucleus ($\sim$1.1 kpc to the southeast), indicating that the gas could already be settled in the disk. J120041, from the Fischer et al. (2018) sample, has a continuum blob at $\sim$ 10kpc to the southwest of the nucleus (assuming the same redshift), that could indicate a recent interaction. The superposition of the gas with a possible origin in different galaxies – that originally have a relative velocity – and their perturbation from the merger, can lead to more than one *narrow* component.

6.1.1 Broad component

We made the hypothesis that the *broad* component is tracing the ionized outflow. The velocity dispersion maps of this component show σ values reaching a maximum of 700–850 km s^{-1} for J094521, J120041 and J135251, while J084135 reaches 400 km s^{-1}, and the remaining galaxies achieve maximum σ values between 450 km,s^{-1} and 650 km s^{-1}, which indicate different degrees of disturbance for each object. Half of the sample has a predominance of negative values in their radial velocities maps, which may be a consequence of dust extinction, since the observed radiation coming from the receding part of the wind travels through a higher amount of dust from the disk (in comparison with the approaching part). However, the other half have a mix of positive and negative velocities, which could indicate that the outflow has larger angle relative to our line-of-sight. Another explanation is that, in these cases, the *broad* profile is unintentionally tracing gas disturbed by mergers.

Regarding the extent of the outflow, the broad component maps show that the region affected by the outflow is more compact than the total region ionized by the AGN. We discuss below the extent of the outflow together with the radial profiles of the mass outflow rates $\dot{M}_{out}$ and power of the outflow $\dot{E}_{out}$ obtained from the broad component.

6.2 Radial profiles of $\dot{M}_{out}$ and $\dot{E}_{out}$

To explore the outflow strength, we plotted $\dot{M}_{out}$ (left) and $\dot{E}_{out}$ (right) radial profiles in Fig. 8. The values of $\dot{M}_{out}$ within the inner few hundred pcs range from 0.1 to $10\,M_\odot\,yr^{-1}$, while the maximum values reach 1 to $10\,M_\odot\,yr^{-1}$ at radii of 1 to 4 kpc. The outflow powers range from 10^{40} to $10^{43}\,erg\,s^{-1}$ in the inner few hundred pcs with maxima between 10^{41} and $10^{43}\,erg\,s^{-1}$. The cases with the lowest $\dot{M}_{out}$ and $\dot{E}_{out}$ values at few hundred pcs show an increase up to 1–2 kpc and then decrease. Three quasars – J082313, J085829 and J094521 – show the most flattened profiles, with variations between the central and most external value lower than a factor of 10. As discussed in Section 6.1, J082313 is not a merger system and J085829 has signs of being a more settled one. Therefore, the absence of interactions could be the reason for an outflow more radially homogeneous. Additionally, J085829 and J094521 are QSOs whose ionization and outflow axes seem to have a higher alignment with our line-of-sight, since their broad component velocity field shows more blueshifts than those of the other sources, and their corresponding flux distributions seem to show a more spherical geometry. The other QSOs present stronger radial variation, with values of $\dot{M}_{out}$ and $\dot{E}_{out}$ varying over $\sim$2 decades, which could indicate a recent peak in its released energy, as expected for interacting systems.

From the radial profiles, we also observe that the outflows reach $\sim$5.5–9.5 kpc in extent (see Table 3). The exception is J094521 – with an extent of only $\sim$2 kpc – that, as we suggested above, has its outflow more directed towards the observer. However, the other object with this characteristic – J085829 – shows an outflow extent of 8 kpc.

6.3 Outflow properties

The maximum values of $\dot{M}_{out}$ and $\dot{E}_{out}$ are listed in Table 3, together with the values of the AGN Bolometric lumionosity (L_{Bol}), feedback efficiency (ε_r) and the radius of the outflow (R_{out}). In order to compare our data with previous results from the literature, we plotted the maximum values of $\dot{M}_{out}$ (left) and $\dot{E}_{out}$ (right) as a function of L_{Bol}, reproducing the Fig. 16 from Shimizu et al. (2019). We used the maximum values instead of an integration over the radius, since rate measurements do not add up radially: they refer to quantities crossing some defined area (spherical shells in our case). The uncertainty bars refer to the difference in the results when using different methods and assumptions (see discussion in Section 6.3.1 and Fig. 10). In order to calculate L_{Bol}, we used the relation from Trump et al. (2015) (Equation 9), with $L_{[O\,III]\lambda5007}$ from Table 1, after being corrected for reddening (Lamastra et al., 2009, Equation 1). The results for our objects are displayed in Fig. 9, along with previous results for other objects from the literature: type II AGNs from Baron e Netzer (2019) and the compiled data by Fiore et al. (2017) and Shimizu et al. (2019). The orange dashed line is the best fit of Fiore et al. (2017) to

Tabela 3 – Outflow properties

Name	$\log(L_{Bol})$	$\log(\dot{M}_{out})$	$\log(\dot{E}_{out})$	$\log(\varepsilon_f)$	R_{out}
(1)	(2)	(3)	(4)	(5)	(6)
J082313	46.68	0.35	41.84	-4.8	9.48
J084135	45.89	0.29	41.43	-4.5	5.76
J085829	46.28	0.79	42.37	-3.9	7.64
J094521	45.82	1.16	43.14	-2.7	2.13
J123006	46.61	0.18	41.20	-4.5	7.13
J135251	46.63	1.06	42.53	-3.3	5.60
J155019	45.71	0.18	41.20	-4.5	7.13
J120041	45.82	1.06	42.53	-3.3	5.60

(1) Galaxy short name; (2) Bolometric luminosity (in units of $\mathrm{erg\,s^{-1}}$);(3) Mass outflow rate (in $\mathrm{M_\odot\,yr^{-1}}$); (4) Outflow power (in $\mathrm{erg\,s^{-1}}$);(5) Feedback efficiency $\varepsilon_f = \dot{E}_{out}/L_{Bol}$.; (6) outflow radius (in kpc).

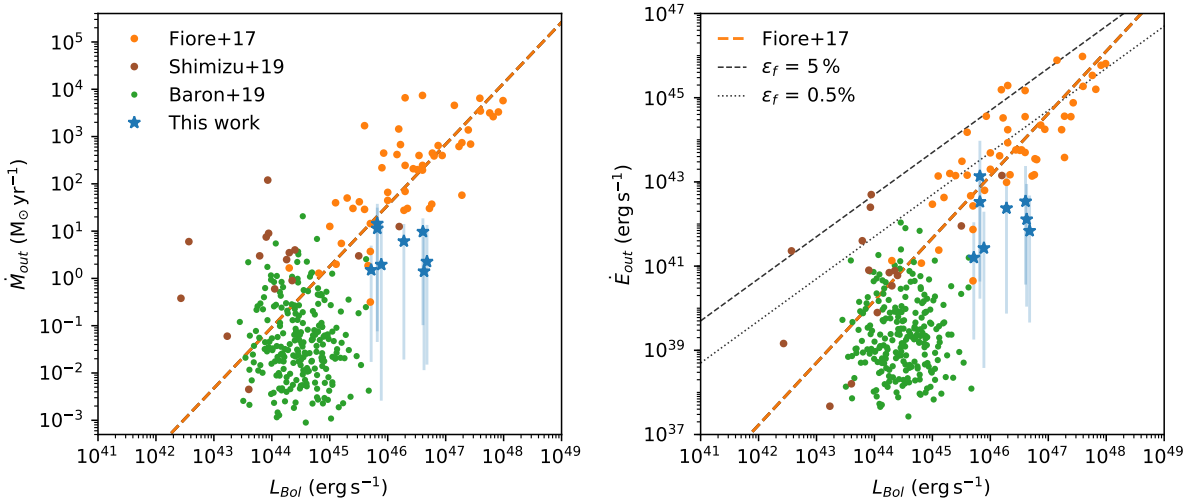

Figura 9 – Mass outflow rate ($\dot{M}_{out}$, left) and outflow power ($\dot{E}_{out}$, right) as a function of the AGN Bolometric luminosity. Our data are presented as blue stars, with the uncertainties corresponding to the variation in the results due to different methods and assumptions (see Fig. 10). Orange circles are the ionized outflows compiled by Fiore et al. (2017); brown circles, the data from Shimizu et al. (2019), and green circles the data from Baron e Netzer (2019). The dashed orange lines are the best fit correlations from Fiore et al. (2017), while the dotted and dashed black lines correspond to outflow feedback efficiencies of 0.5% and 5%, respectively.

their ionized outflows data. Our sample has average values of $\dot{M}_{out} = 6.1 \pm 4.8\,\mathrm{M_\odot\,yr^{-1}}$ and $\dot{E}_{out} = (3.2 \pm 4.2) \times 10^{42}\,\mathrm{erg\,s^{-1}}$.

As shown in Fig. 9, our QSOs consistently fall below the Fiore et al. (2017) best fit relations (orange dashed lines). This is not necessarily an inconsistency, as our 8 objects are still approximately located in the plots within the scatter observed for the points used to obtain the fit (orange circles). The location of the Shimizu et al. (2019) (brown) and

Baron e Netzer (2019) (green) points are also displaced relative to the trend lines, being respectively above and below the relation, on average. However, the calculation methods of $\dot{M}_{out}$ and $\dot{E}_{out}$, for the different works cited above are not equal: Fiore et al. (2017) used homogeneous assumptions to redo the calculations of their retrieved data from literature; (Shimizu et al., 2019) compiled low-luminosity quasars data from literature, that have varied methods of analysis; (Baron; Netzer, 2019) use a different method, involving SED fitting and SDSS single spectra measurements.

6.3.1 Influence of different calculation methods and assumptions

In Fig. 10, we tested the influence of different methods/assumptions in the calculation of $\dot{M}_{out}$ and $\dot{E}_{out}$. First, we tested the effect of some of the differences between our method and that of Fiore et al. (2017). In our case, we used the luminosity of the *broad* component to obtain the mass of the ionized wind ($M_{\rm H\,II}$), while Fiore et al. (2017) use the total flux. Hence, we recalculated the outflow properties (Eqs. 4.5 and 4.6), with a mass $M_{\rm H\,II}$ (Eq. 4.3) obtained from the integrated flux of all components (*broad* + *narrows*), and plotted the results as red diamonds in Fig. 10. Since both $\dot{M}_{out}$ and $\dot{E}_{out}$ depend linearly on $M_{\rm H\,II}$, their values became higher, in better agreement with the trend line (orange), with higher average values $\dot{M}_{out} = 18 \pm 11\,{\rm M}_\odot$ and $\dot{E}_{out} = (8.6 \pm 9.3) \times 10^{42}\,{\rm erg\,s^{-1}}$. We then tested the effect of a constant density, repeating our calculations using a value of $n_e = 200\,{\rm cm^{-3}}$, as used by Fiore et al. (2017). The outcome (black triangles) did not differ much from our original results (blue stars), having similar average values: $\dot{M}_{out} = 5.6 \pm 5.1\,{\rm M}_\odot$ and $\dot{E}_{out} = (2.5 \pm 2.4) \times 10^{42}\,{\rm erg\,s^{-1}}$. This can be explained by the fact that the average density of our sample ($n_e = 240 \pm 60\,{\rm cm^{-3}}$) is close to the fixed value adopted by Fiore et al. (2017).

Recently, many studies started to point out problems with the use of [S II]$\lambda\lambda$6718,31 to obtain the density of the outflowing ionized gas (Harrison et al., 2018), suggesting this diagnostic results in smaller values of n_e than the values typical of the outflows. (Rose et al., 2018), using trans-auroral lines of [O II]$\lambda\lambda$7319,31 and [S II]$\lambda\lambda$4068,76 found densities between $10^{3.4} - 10^{4.8}\,{\rm cm^{-3}}$, one to two orders of magnitude higher than the values obtained from [S II]. Using a method that involves the extent of the outflow and the ionization parameter U, Baron e Netzer (2019) obtained values in the range $n_e \sim 10^3 - 10^6\,{\rm cm^{-3}}$. One of the reasons for this discrepancy is that the [S II]$\lambda\lambda$6718,31 ratio is only sensitive to n_e in the range of $10 - 10^4\,{\rm cm^{-3}}$, with high uncertainties at the extreme values. Another problem is that the ionization potential of [S II] (10.36 eV) is lower than that of [O III](35.1 eV), a line frequently used as a tracer of the gas in outflow. Therefore, [S II] may originate from other regions in the galaxy, since the source of ionization may not be the same. A possible solution is the use of [Ar IV]$\lambda\lambda$4011,40 emission lines – that have a potential energy $[Ar\,III] \rightarrow [Ar\,IV]$ of 40.7 eV (Proxauf; Öttl; Kimeswenger, 2014). However, its

small S/N ratio is an obstacle. In order to evaluate the effect of a higher electron density, we recalculated the outflow properties, using the average value obtained by Baron e Netzer (2019): $n_e = 10^{4.5}\,\mathrm{cm}^{-3}$. The result is plotted as grey circles in Fig. 10, and its average values are $\dot{M}_{out} = (3.6 \pm 3.3)\times10^{-2}\,\mathrm{M}_\odot$ and $\dot{E}_{out} = (1.5 \pm 1.5)\times10^{40}\,\mathrm{erg\,s}^{-1}$. Since both quantities have a inverse dependence on n_e (see Eqs. 4.3–4.6), it was expected that the values would decrease by two orders of magnitude ($10^{4.5}\,\mathrm{cm}^{-3}/240\,\mathrm{cm}^{-3} \sim 10^2$).

Due to projection effects – from the possible varying orientations (i) of the outflow in the plane of the sky – the velocities and distances measurements are biased, resulting in smaller observed values. The deprojected quantities (v_0 and Δr_0) are obtained by: $v_0 = v_{obs}/sin(i)$ and $\Delta r_0 = \Delta r_{obs}/cos(i)$, where v_{obs} and Δr_{obs} are their observed values. We recalculate $\dot{M}_{out}$ and $\dot{E}_{out}$, applying these corrections for v_{out} and δr with $i = 30,\ 45$ and 60°, and added the results to Fig. 10 as purple crosses ($i = 45°$) with errorbars referring to the differences obtained for $i = 30$ and 60°. We deprojected δr because we wanted to keep the 2 pixel width of the annulus. Since the deprojected width increases, the time taken to cross it ($t = v_{out}/\delta r$) also increases, decreasing $\dot{M}_{out}$. We could also compute the outflow properties using the original projected value of δr in kpc. In this case, the width of the annulus would remain the same, although we would need to lower the number of pixels used. Therefore, deprojecting both quantities, their values gain a dependence of: $\dot{M}_{out} \propto v_{out}/\delta r \propto [\cos(i)/\sin(i)]$ and $\dot{E}_{out} \propto v_{out}^3/\delta r \propto [\cos(i)/\sin^3(i)]$. Consequently, $\dot{M}_{out}$ decreases for $i > 45°$ and increases for values below, reaching $\dot{M}_{out} = 10 \pm 0.8\,\mathrm{M}_\odot$, for $i = 30°$. For $\dot{E}_{out}$, the turning point happens at $i \sim 55°$, resulting in an average value of $\dot{E}_{out} = (2.1 \pm 2.9)\times10^{43}\,\mathrm{erg\,s}^{-1}$, for $i = 30°$.

6.3.2 Feedback efficiency

In studies about the impact of AGNs in their host galaxies, the feedback efficiency ($\varepsilon_f = \dot{E}_{out}/L_{Bol}$) is often obtained, since it has been suggested that its value may define if the power of the outflow is high enough to affect the evolution of the host galaxy. Using simulations of galaxy mergers as triggers of AGNs, Di Matteo, Springel e Hernquist (2005) found that a value of $\varepsilon_f = 5\%$ reproduces the $M_{BH} - \sigma_*$ relation. Other authors (Hopkins; Elvis, 2010), assuming that the feedback only needs to drive winds on the hot gas, that subsequently affects the cold part, found $\varepsilon_f = 0.5\%$, an order of magnitude lower. We added both efficiency thresholds in Fig. 9, as black lines ($\dot{E}_{out} = \epsilon_f\, L_{Bol}$). We can see that only part of the most luminous quasars ($L_{Bol} \gtrsim 10^{45}\,\mathrm{erg\,s}^{-1}$) are able to achieve the required efficiency from Hopkins e Elvis (2010). In particular, our entire sample is below $\varepsilon_f = 0.5\%$.

Finally, we would like to point out that feedback from AGN do not comprise only ionized gas outflows. As pointed out previously by Harrison et al. (2018), ε_f determined from ionized outflows only, may not reproduce the simulations, since only a fraction of the

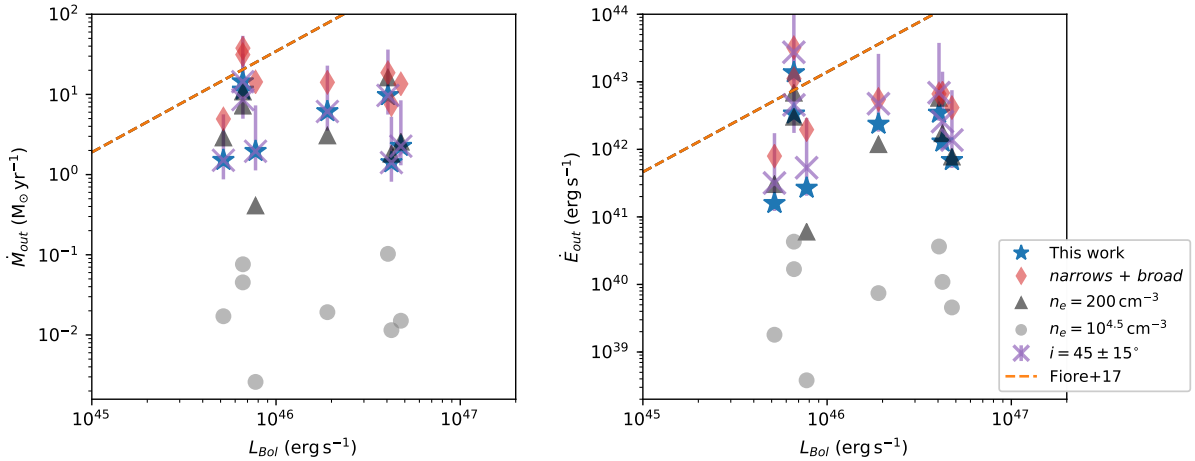

Figura 10 – Variation in the outflow energetics, based on different assumptions. The blue circles are the method used in this work, where only the *broad* component was used to obtain the $M_{\mathrm{H\,II}}$ involved, and a constant electron density was assumed. The black triangles and grey circles were obtained for a constant $n_e = 200\,\mathrm{cm}^{-3}$ and $n_e = 10^{4.5}\,\mathrm{cm}^{-3}$. respectively. The red diamonds are the resulting values for method , using both *narrow* and *broad* components instead. The purple crosses are the effect of deprojection for an inclination of $i = 45°$, with uncertainties being the result of $i = 30$ and $60°$ values.

energy deposited in the ISM by the AGN may actually induce outflow dynamics. Other forms of feedback may be present, such as the feedback from radiation. In addition, the ionized phase is only a fraction of the gas present: Fiore et al. (2017) found that molecular winds contribute more to the energy released in the feedback, although ionized winds increase its impact for higher L_{Bol}. Hence, these effects may explain our lower efficiencies in comparison to the predicted by models.

7 Conclusões

Através de uso de técnicas de Espectroscopia de Campo Integral (IFS), é possível estudar propriedades relacionadas ao *feedback* de Núcleo Ativos de Galáxias (AGN). Neste trabalho, utilizamos esta técnica para analisar uma amostra de 8 quasares tipo II, através do instrumento GMOS-IFU do Telescópio Gemini. Esses objetos possuem redshifts no intervalo $0.1 < z < 0.5$ e e luminosidades bolométricas entre $10^{45} < L_{Bol} < 10^{47}\,\mathrm{erg\,s^{-1}}$. Utilizamos entre 1 e 4 gaussianas para modelar os perfis de densidade de fluxo das linhas de emissão provenientes da NLR. Definimos uma componente – chamada de *broad* – como a que possui a maior dispersão de velocidades. Por trás desta definição, está a hipótese de que essa componente representa o gás em *outflow*, visto que a sua dispersão de velocidade indica que este é o gás mais perturbado cinematicamente, consistente com o que e esperado de um *outflow*. As outras componentes (*narrow* 1, *narrow* 2, etc) representam o gás em órbita no disco da galáxia e/ou remanescente de uma interação – prévia ou em andamento – com uma galáxia vizinha. As Figuras 11–18 mostram os resultados dos ajustes. Os principais resultados foram:

- ◇ O uso de até 3 gaussianas *narrow* em alguns objetos sinaliza que estamos vendo o gás proveniente de mais que uma galáxia, que com a pertubação causada, resulta em mais que uma componente estreita. Os mapas (Figuras 7 e 19–25) mostram cenários complexos para a distribuição do fluxo e para a cinemática do gás, resultantes desta superposição de diferentes componentes.

- ◇ A dispersão de velocidade do gás em *outflow* atinge máximos de $\sim 850\,\mathrm{km\,s^{-1}}$ para alguns objetos, condizentes com a hipótese de que este gás está perturbado por *outflows* que contribuem para o *feedback* dos AGNs.

- ◇ As extensões do gás ionizado em *outflow* variam entre ~ 5.5–$9.5\,\mathrm{kpc}$, com exceção do quasar J094521, com $\sim 2\,\mathrm{kpc}$ (Figura 8). As extensões dessas componentes *broad* são sempre menores que as *narrow*, sugerindo que os ventos não atingem as extremidades das regiões ocupadas pelo gás ionizado.

- ◇ A partir das massas de gás obtidas da luminosidade da componente *broad* de Hα, calculamos a taxa de massa em *outflow* ($\dot{M}_{out}$) em função do raio (Figura 8), e obtivemos valores entre 0.1 e $10\,\mathrm{M_\odot\,yr^{-1}}$ para até 4 kpc do núcleo. Para distâncias maiores, as taxas decaem, chegando a valores entre 1 e $10^{-3}\,\mathrm{M_\odot\,yr^{-1}}$.

- ◇ Calculamos a potência cinética do *outflow* ($\dot{E}_{out}$) e obtivemos valores máximos entre 10^{41} e $10^{43}\,\mathrm{erg\,s^{-1}}$ para até 4 kpc do núcleo (Figura 8). Correspondendo a

$\sim 0.1 - 0.001\,\%$ de L_{Bol}, estes valores estão abaixo de 0.5-5 % (Hopkins; Elvis, 2010; Di Matteo; Springel; Hernquist, 2005): valores usualmente considerados como necessários para associar o *feedback* dos AGNs com efeitos de supressão de formação estelar na evolução das galáxias.

- ◇ Tanto of valores de $\dot{M}_{out}$ como de $\dot{E}_{out}$, quando comparados com L_{Bol} (Figura 9), ficam dentro da dispersão apresentada pelas relações encontradas por Fiore et al. (2017), muito embora os valores médios – $\dot{M}_{out} = 6.1 \pm 4.8\,M_\odot$ e $\dot{E}_{out} = (3.2 \pm 4.2) \times 10^{42}\,\mathrm{erg\,s^{-1}}$ – fiquem sistematicamente abaixo da relação.

- ◇ Investigamos o papel de diferentes hipóteses adotadas no cálculo de $\dot{M}_{out}$ como de $\dot{E}_{out}$ (Figura 10), e mostramos que, ao considerarmos a hipótese de que todo o gás está em *outflow* (como adotado em trabalhos anteriores), e não somente a componente *broad*, os valores se aproximam mais da relação de Fiore et al. (2017). Por outro lado, se considerarmos que a densidade do gás em *outflow* deve ser maior que a adotada, conforme estudos recentes (Baron; Netzer, 2019, por exemplo), os valores destas quantidades diminuem por duas ordens de magnitude.

- ◇ Finalmente, levantamos o ponto de que o *feedback* obtido através do gás ionizado é somente parte do total produzido pelos AGNs. Outras fases do gás, como a molecular e neutra, estão presentes. Além disso, a energia liberada pode se manifestar de outras formas – além da energia cinética do *outflow*. Exemplos são a radiação que ionizada grande parte do gás presente (Storchi-Bergmann et al., 2018), e o trabalho gasto para superar o potencial gravitacional (Harrison et al., 2018).

Perspectivas futuras: Para complementar a avaliação do feedback de AGNs, futuramente desejamos mapear e estudar este *feedback* do gás na fase molecular, visto que muitos autores argumentam que esta é a fase que mais contribui para o *feedback* mecânico, na forma de energia cinética dos outflows. Isto pode ser feito através de observações em rádio com o Observatório ALMA (*Atacama Large Millimeter/submillimeter Array*). Possuímos também interesse em obter espectroscopia de alta resolução e S/N para os nossos objetos ou uma amostra semelhante com um maior S/N em regiões espectrais que possuam linhas sensíveis para altas densidades. Ou seja, que sejam menos enviesadas – do que as linhas de [S II] que utilizamos – para valores de densidade mais baixa, que podem não ser representativas dos outflows. Instrumentos como o MUSE do VLT (*Very Large Telescope*) poderiam ser adequados para este estudo.

Trabalhos adicionais realizados

- Co-autoria no artigo Storchi-Bergmann et al. (2018), para o qual trabalhei na redução e análise dos dados, e na produção das figuras.
- Participação no desenvolvimento de rotinas de redução de dados de espectroscopia de campo integral para o programa GIREDS[1], de Daniel Ruschel Dutra.

[1] <https://bitbucket.org/danielrd6/gireds>

Referências

Allington-Smith, J. et al. Integral Field Spectroscopy with the Gemini Multiobject Spectrograph. I. Design, Construction, and Testing. *Astrophysical Journal, Letters*, v. 114, n. 798, p. 892–912, Aug 2002. Citado na página 19.

Antonucci, R. Unified models for active galactic nuclei and quasars. *Annual Review of Astronomy and Astrophysics*, v. 31, p. 473–521, 1993. Citado na página 12.

Audibert, A. et al. Probing the active galactic nucleus unified model torus properties in Seyfert galaxies. *Monthly Notices of the RAS*, v. 464, n. 2, p. 2139–2173, jan. 2017. Citado na página 12.

B. Saxton NRAO/AUI/NSF. *A Unified AGN Model*. <https://public.nrao.edu/gallery/a-unified-agn-model/>. Accessed: 10-03-2020. Nenhuma citação no texto.

Baron, D.; Netzer, H. Discovering AGN-driven winds through their infrared emission - II. Mass outflow rate and energetics. *Monthly Notices of the RAS*, v. 486, n. 3, p. 4290–4303, Jul 2019. Citado 6 vezes nas páginas 6, 33, 34, 35, 36 e 39.

Bennert, N. et al. Size and Structure of the Narrow-Line Region of Quasars. *ApJL*, v. 574, p. L105–L109, ago. 2002. Citado 2 vezes nas páginas 14 e 15.

Ciotti, L.; Ostriker, J. P.; Proga, D. Feedback from Central Black Holes in Elliptical Galaxies. III. Models with Both Radiative and Mechanical Feedback. *Astrophysical Journal*, v. 717, n. 2, p. 708–723, Jul 2010. Citado na página 14.

Croton, D. J. et al. Semi-Analytic Galaxy Evolution (SAGE): Model Calibration and Basic Results. *Astrophysical Journal, Supplement*, v. 222, n. 2, p. 22, Feb 2016. Citado na página 13.

Di Matteo, T.; Springel, V.; Hernquist, L. Energy input from quasars regulates the growth and activity of black holes and their host galaxies. *Nature*, v. 433, n. 7026, p. 604–607, Feb 2005. Citado 2 vezes nas páginas 36 e 39.

Elitzur, M. On the Unification of Active Galactic Nuclei. *ApJL*, v. 747, p. L33, mar. 2012. Citado na página 12.

Event Horizon Telescope Collaboration et al. First M87 Event Horizon Telescope Results. I. The Shadow of the Supermassive Black Hole. *ApJL*, v. 875, n. 1, p. L1, Apr 2019. Citado na página 11.

Fabian, A. C. Observational Evidence of Active Galactic Nuclei Feedback. *Annual Review of Astronomy and Astrophysics*, v. 50, p. 455–489, Sep 2012. Citado na página 13.

Ferrarese, L.; Merritt, D. A Fundamental Relation between Supermassive Black Holes and Their Host Galaxies. *ApJL*, v. 539, p. L9–L12, ago. 2000. Citado na página 14.

Feruglio, C. et al. The multi-phase winds of Markarian 231: from the hot, nuclear, ultra-fast wind to the galaxy-scale, molecular outflow. *Astronomy and Astrophysics*, v. 583, p. A99, Nov 2015. Citado na página 14.

Fiore, F. et al. AGN wind scaling relations and the co-evolution of black holes and galaxies. *Astronomy and Astrophysics*, v. 601, p. A143, May 2017. Citado 8 vezes nas páginas 6, 15, 27, 33, 34, 35, 37 e 39.

Fischer, T. C. et al. Hubble Space Telescope Observations of Extended [O III]λ 5007 Emission in Nearby QSO2s: New Constraints on AGN Host Galaxy Interaction. *Astrophysical Journal*, v. 856, n. 2, p. 102, Apr 2018. Citado 3 vezes nas páginas 18, 23 e 32.

Fixsen, D. J. et al. The Cosmic Microwave Background Spectrum from the Full COBE FIRAS Data Set. *Astrophysical Journal*, v. 473, p. 576, Dec 1996. Citado na página 18.

Gonzalez-Perez, V. et al. How sensitive are predicted galaxy luminosities to the choice of stellar population synthesis model? *Monthly Notices of the RAS*, v. 439, n. 1, p. 264–283, Mar 2014. Citado na página 13.

Harrison, C. M. et al. Kiloparsec-scale outflows are prevalent among luminous AGN: outflows and feedback in the context of the overall AGN population. *Monthly Notices of the RAS*, v. 441, n. 4, p. 3306–3347, Jul 2014. Citado 2 vezes nas páginas 14 e 22.

Harrison, C. M. et al. AGN outflows and feedback twenty years on. *Nature Astronomy*, v. 2, p. 198–205, Feb 2018. Citado 4 vezes nas páginas 14, 35, 36 e 39.

Heckman, T. M.; Best, P. N. The Coevolution of Galaxies and Supermassive Black Holes: Insights from Surveys of the Contemporary Universe. *Annual Review of Astronomy and Astrophysics*, v. 52, p. 589–660, ago. 2014. Citado 2 vezes nas páginas 13 e 14.

Hopkins, P. F.; Elvis, M. Quasar feedback: more bang for your buck. *Monthly Notices of the RAS*, v. 401, n. 1, p. 7–14, Jan 2010. Citado 2 vezes nas páginas 36 e 39.

Husemann, B. et al. Large-scale outflows in luminous QSOs revisited. The impact of beam smearing on AGN feedback efficiencies. *Astronomy and Astrophysics*, v. 594, p. A44, Oct 2016. Citado na página 14.

Karouzos, M.; Woo, J.-H.; Bae, H.-J. Unraveling the Complex Structure of AGN-driven Outflows. I. Kinematics and Sizes. *Astrophysical Journal*, v. 819, p. 148, mar. 2016. Citado na página 14.

Lamastra, A. et al. The bolometric luminosity of type 2 AGN from extinction-corrected [OIII]. No evidence of Eddington-limited sources. *Astronomy and Astrophysics*, v. 504, n. 1, p. 73–79, Sep 2009. Citado na página 33.

Lena, D. et al. The Complex Gas Kinematics in the Nucleus of the Seyfert 2 Galaxy NGC 1386: Rotation, Outflows, and Inflows. *Astrophysical Journal*, v. 806, p. 84, jun. 2015. Citado na página 14.

Liu, G. et al. Observations of feedback from radio-quiet quasars - I. Extents and morphologies of ionized gas nebulae. *Monthly Notices of the RAS*, v. 430, n. 3, p. 2327–2345, Apr 2013. Citado 2 vezes nas páginas 14 e 22.

Man, A.; Belli, S. Star formation quenching in massive galaxies. *Nature Astronomy*, v. 2, p. 695–697, Sep 2018. Citado na página 14.

Marconi, A.; Hunt, L. K. The Relation between Black Hole Mass, Bulge Mass, and Near-Infrared Luminosity. *ApJL*, v. 589, p. L21–L24, maio 2003. Citado na página 14.

Nelson, D. et al. First results from the TNG50 simulation: galactic outflows driven by supernovae and black hole feedback. *Monthly Notices of the RAS*, v. 490, n. 3, p. 3234–3261, Dec 2019. Citado na página 13.

Nenkova, M. et al. AGN Dusty Tori. I. Handling of Clumpy Media. *Astrophysical Journal*, v. 685, n. 1, p. 147–159, set. 2008. Citado na página 12.

Netzer, H. Revisiting the Unified Model of Active Galactic Nuclei. *Annual Review of Astronomy and Astrophysics*, v. 53, p. 365–408, ago. 2015. Citado na página 12.

Osterbrock, D. E.; Ferland, G. J. *Astrophysics of gaseous nebulae and active galactic nuclei*. [S.l.: s.n.], 2006. Citado 3 vezes nas páginas 25, 26 e 27.

Peterson, B. M. *An Introduction to Active Galactic Nuclei*. [S.l.: s.n.], 1997. Citado na página 11.

Proxauf, B.; Öttl, S.; Kimeswenger, S. Upgrading electron temperature and electron density diagnostic diagrams of forbidden line emission. *Astronomy and Astrophysics*, v. 561, p. A10, Jan 2014. Citado 3 vezes nas páginas 25, 26 e 35.

Ramos Almeida, C.; Ricci, C. Nuclear obscuration in active galactic nuclei. *Nature Astronomy*, v. 1, p. 679–689, out. 2017. Citado na página 12.

Revalski, M. et al. Quantifying Feedback from Narrow Line Region Outflows in Nearby Active Galaxies. I. Spatially Resolved Mass Outflow Rates for the Seyfert 2 Galaxy Markarian 573. *Astrophysical Journal*, v. 856, n. 1, p. 46, Mar 2018. Citado na página 26.

Reyes, R. et al. Space Density of Optically Selected Type 2 Quasars. *Astronomical Journal*, v. 136, p. 2373–2390, dez. 2008. Citado 2 vezes nas páginas 18 e 29.

Rose, M. et al. Quantifying the AGN-driven outflows in ULIRGs (QUADROS) - I: VLT/Xshooter observations of nine nearby objects. *Monthly Notices of the RAS*, v. 474, n. 1, p. 128–156, Feb 2018. Citado na página 35.

Rupke, D. S. N.; Veilleux, S. The Multiphase Structure and Power Sources of Galactic Winds in Major Mergers. *Astrophysical Journal*, v. 768, n. 1, p. 75, May 2013. Citado na página 27.

Savage, B. D.; Mathis, J. S. Observed properties of interstellar dust. *Annual Review of Astronomy and Astrophysics*, v. 17, p. 73–111, Jan 1979. Citado na página 26.

Schaye, J. et al. The EAGLE project: simulating the evolution and assembly of galaxies and their environments. *Monthly Notices of the RAS*, v. 446, n. 1, p. 521–554, Jan 2015. Citado na página 13.

Schmidt, M. 3C 273 : A Star-Like Object with Large Red-Shift. *Nature*, v. 197, n. 4872, p. 1040, Mar 1963. Citado na página 11.

Schmitt, H. R. et al. A Hubble Space Telescope Survey of Extended [O III] λ5007 Å Emission in a Far-Infrared-Selected Sample of Seyfert Galaxies: Results. *Astrophysical Journal*, v. 597, p. 768–779, nov. 2003. Citado na página 14.

Schmitt, H. R. et al. A Hubble Space Telescope Survey of Extended [O III] λ5007 Emission in a Far-Infrared Selected Sample of Seyfert Galaxies: Observations. *Astrophysical Journal, Supplement*, v. 148, p. 327–352, out. 2003. Citado na página 15.

Schnorr-Müller, A. et al. Feeding and feedback in the inner kiloparsec of the active galaxy NGC 2110. *Monthly Notices of the RAS*, v. 437, p. 1708–1724, jan. 2014. Citado na página 14.

Seyfert, C. K. Nuclear Emission in Spiral Nebulae. *Astrophysical Journal*, v. 97, p. 28, Jan 1943. Citado na página 11.

Shimizu, T. T. et al. The multiphase gas structure and kinematics in the circumnuclear region of NGC 5728. *Monthly Notices of the RAS*, v. 490, n. 4, p. 5860–5887, Dec 2019. Citado 5 vezes nas páginas 6, 27, 33, 34 e 35.

Silk, J.; Mamon, G. A. The current status of galaxy formation. *Research in Astronomy and Astrophysics*, v. 12, n. 8, p. 917–946, Aug 2012. Citado na página 13.

Somerville, R. S.; Davé, R. Physical Models of Galaxy Formation in a Cosmological Framework. *Annual Review of Astronomy and Astrophysics*, v. 53, p. 51–113, Aug 2015. Citado na página 13.

Storchi-Bergmann, T. et al. Bipolar Ionization Cones in the Extended Narrow-line Region of Nearby QSO2s. *Astrophysical Journal*, v. 868, n. 1, p. 14, Nov 2018. Citado 8 vezes nas páginas 14, 15, 18, 23, 26, 32, 39 e 40.

Storchi-Bergmann, T.; Schnorr-Müller, A. Observational constraints on the feeding of supermassive black holes. *Nature Astronomy*, v. 3, p. 48–61, Jan 2019. Citado na página 13.

Tody, D. The IRAF Data Reduction and Analysis System. In: _____. *IN: Instrumentation in astronomy VI; Proceedings of the Meeting, Tucson, AZ, Mar. 4-8, 1986. Part 2 (A87-36376 15-35). Bellingham, WA, Society of Photo-Optical Instrumentation Engineers, 1986, p. 733.* [S.l.: s.n.], 1986. (Society of Photo-Optical Instrumentation Engineers (SPIE) Conference Series, v. 627), p. 733. Citado na página 23.

Treister, E. et al. Major Galaxy Mergers Only Trigger the Most Luminous Active Galactic Nuclei. *ApJL*, v. 758, n. 2, p. L39, Oct 2012. Citado na página 18.

Trump, J. R. et al. The Biases of Optical Line-Ratio Selection for Active Galactic Nuclei and the Intrinsic Relationship between Black Hole Accretion and Galaxy Star Formation. *Astrophysical Journal*, v. 811, n. 1, p. 26, Sep 2015. Citado na página 33.

Wright, E. L. A Cosmology Calculator for the World Wide Web. *Astrophysical Journal, Letters*, v. 118, n. 850, p. 1711–1715, Dec 2006. Citado na página 18.

APÊNDICE A – Additional figures

Additional material which would interrupt the flow of the main paper.

A.1 Examples of emission-line fitting results

Examples of the fitting results for the QSOs of our sample.

A.2 Maps of flux distributions and gas kinematics

Maps of the parameters obtained in the emission-line fitting process. They are analogous to Fig. 7.

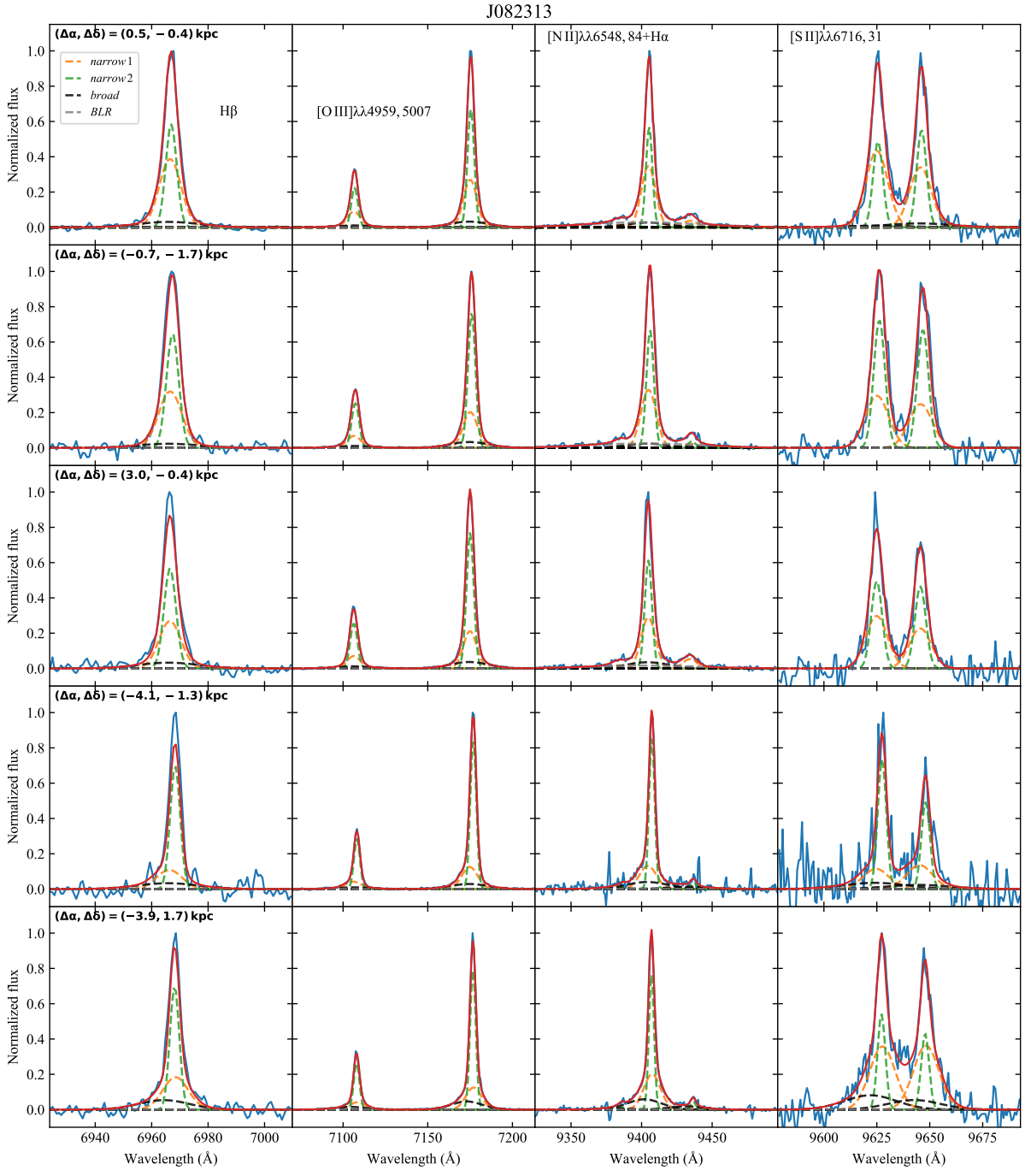

Figura 11 – Fitting results for a few spectra of J082313. Each line of the figure corresponds to a different position, which has its value relative to the nucleus identified in the upper left corner of the first column panels.

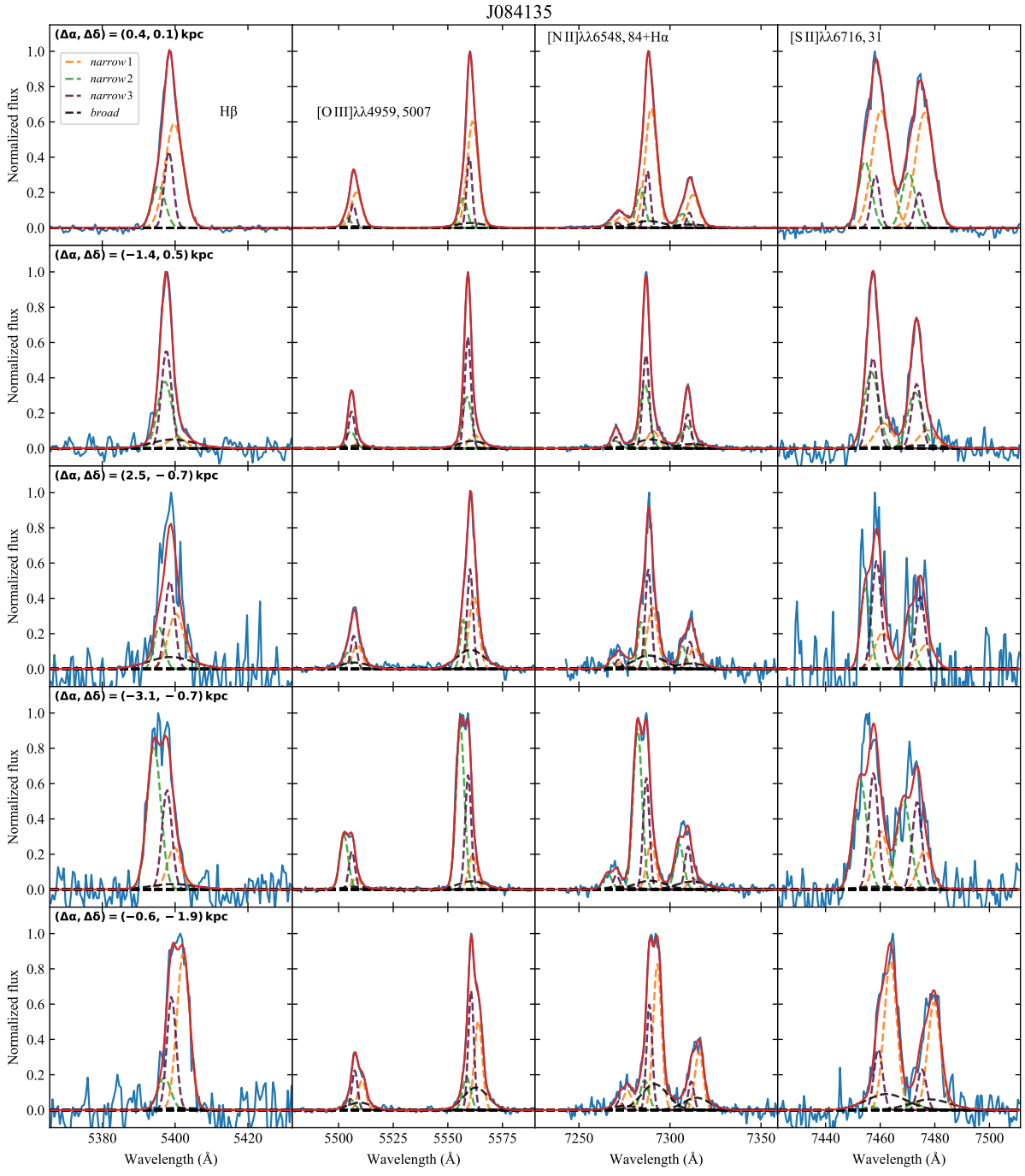

Figura 12 – Same as Fig. 19 but for J084135.

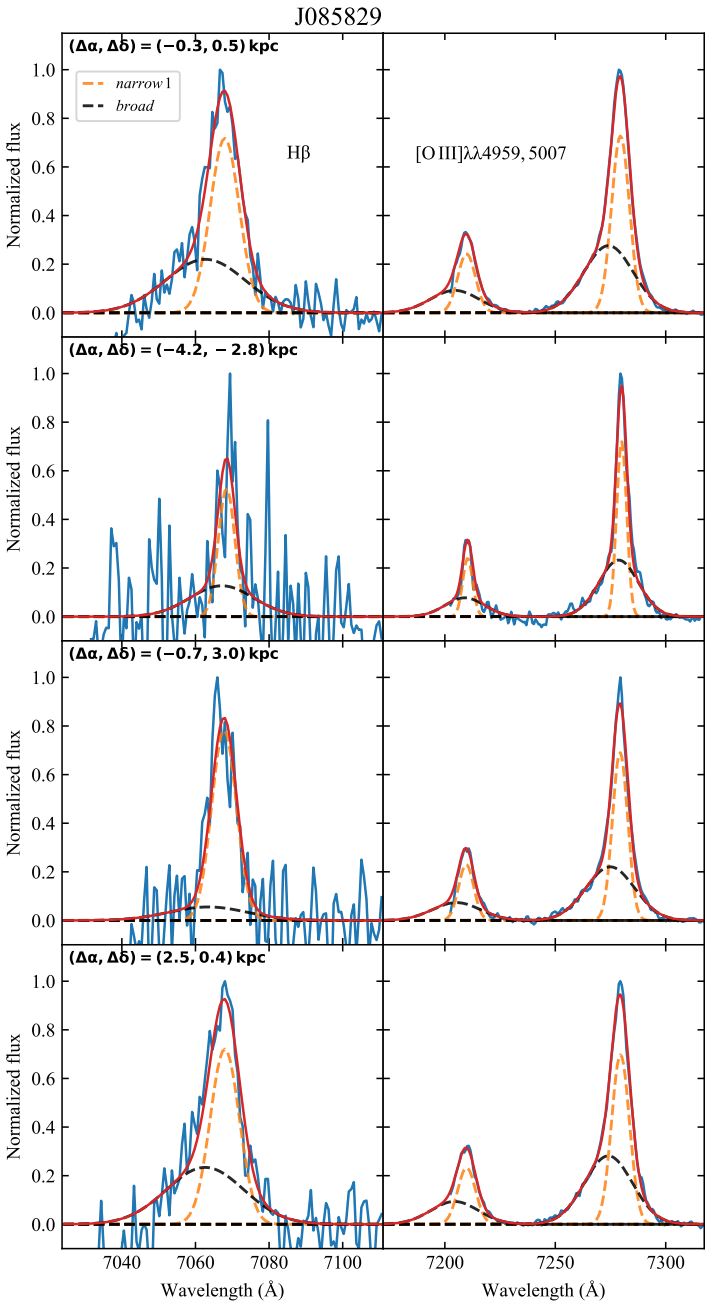

Figura 13 – Same as Fig. 19 but for J085829.

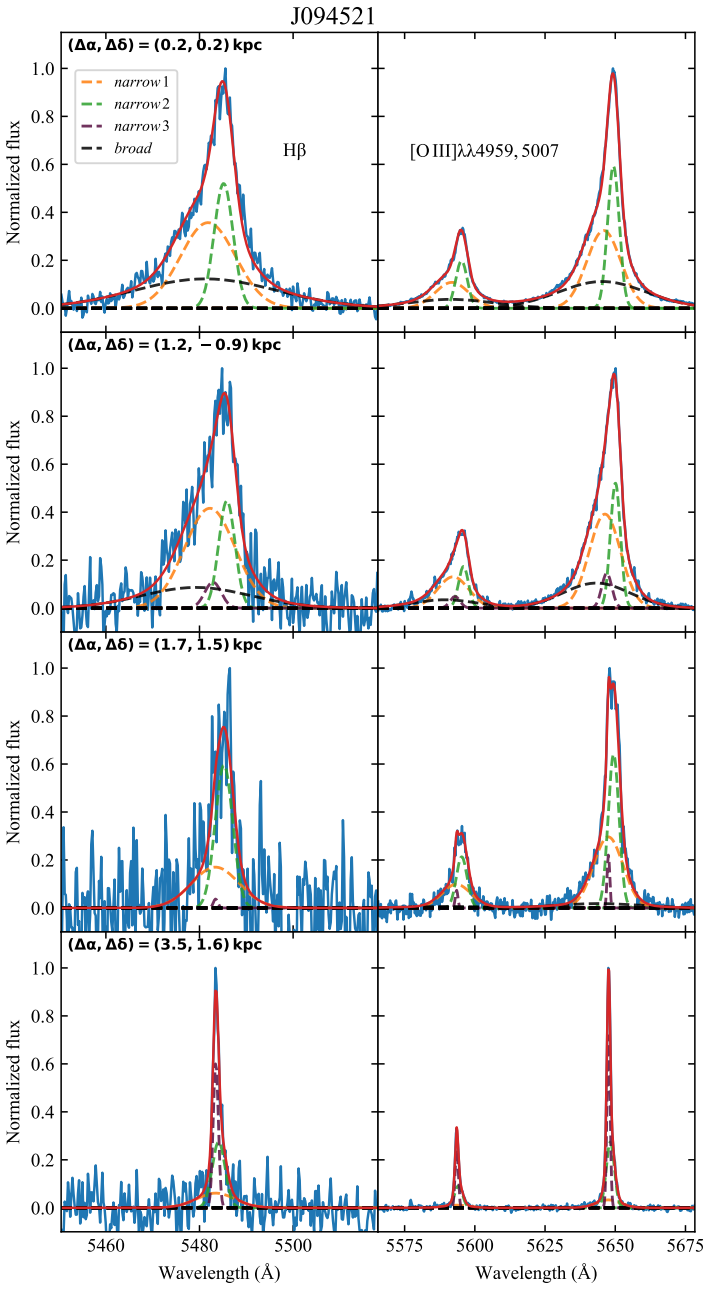

Figura 14 – Same as Fig. 19 but for J094521.

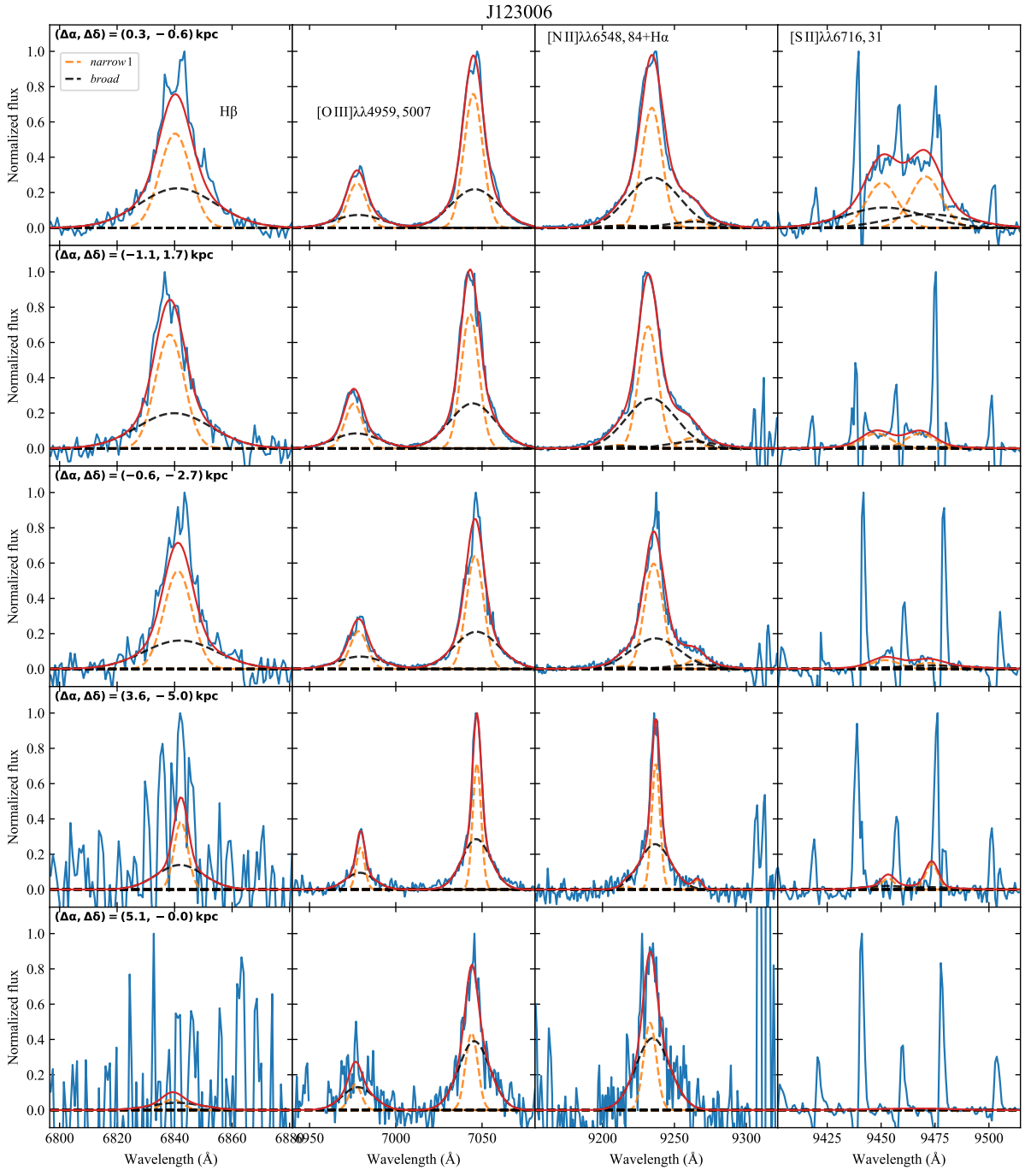

Figura 15 – Same as Fig. 19 but for J123006.

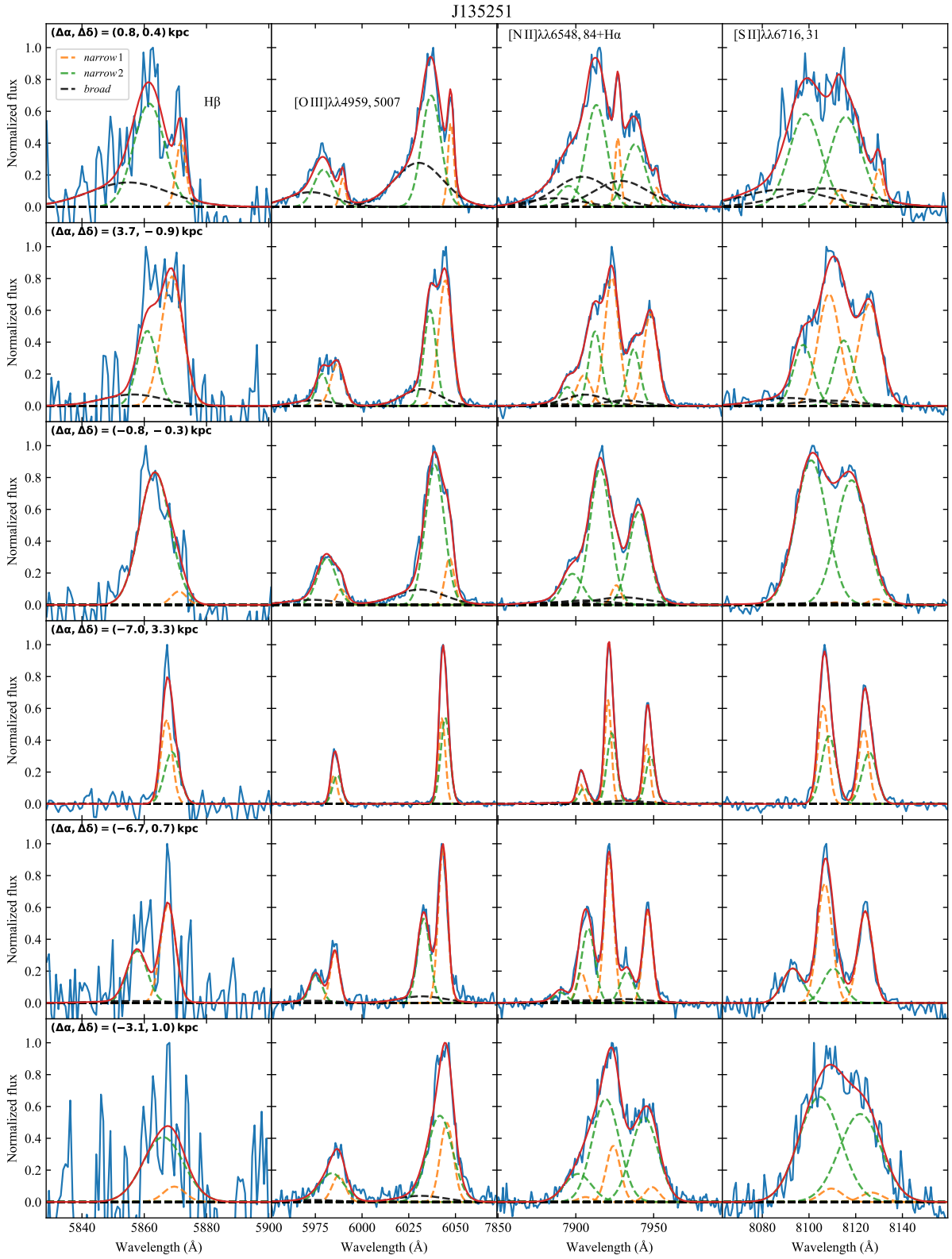

Figura 16 – Same as Fig. 19 but for J135251.

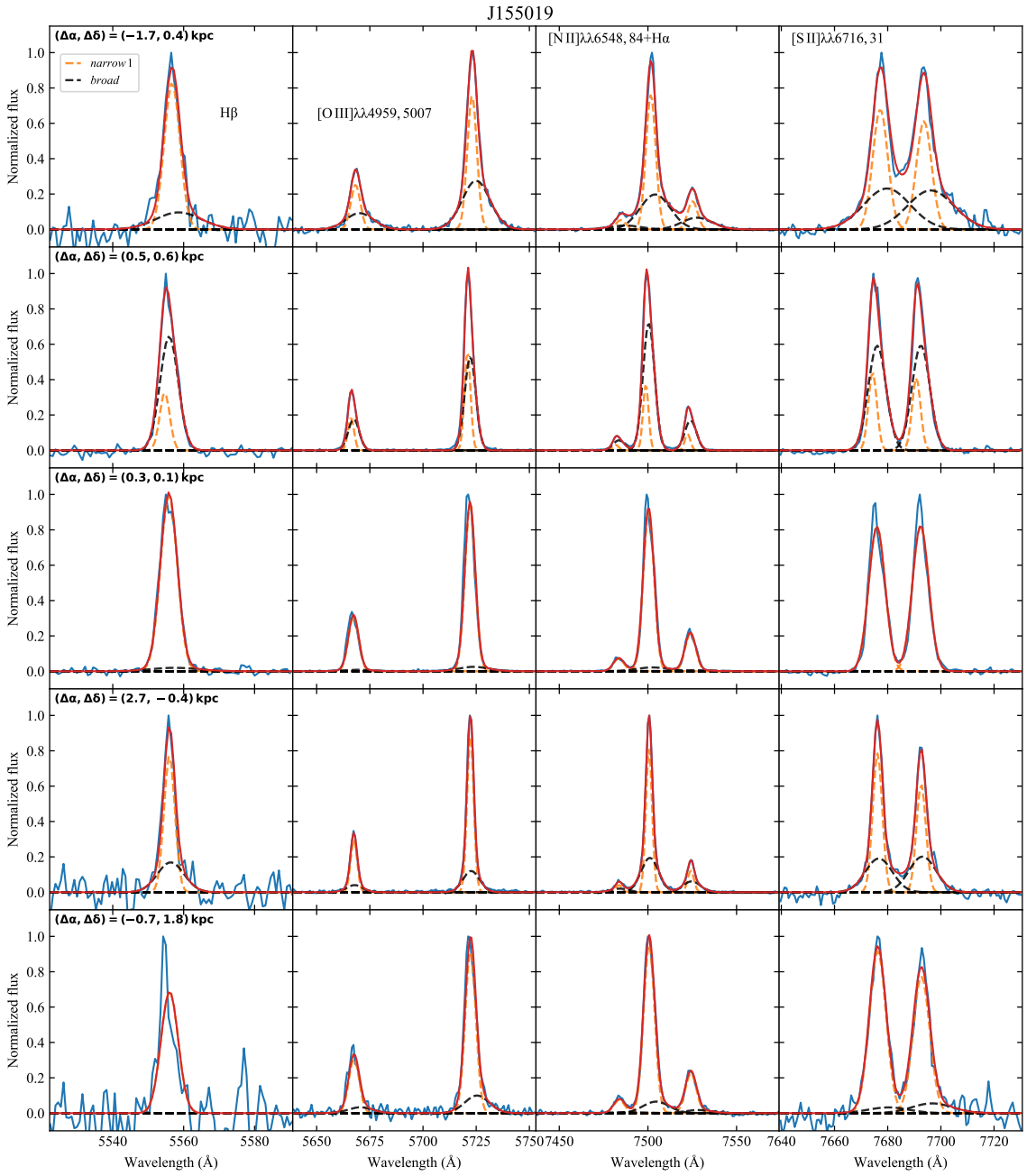

Figura 17 – Same as Fig. 19 but for J155019.

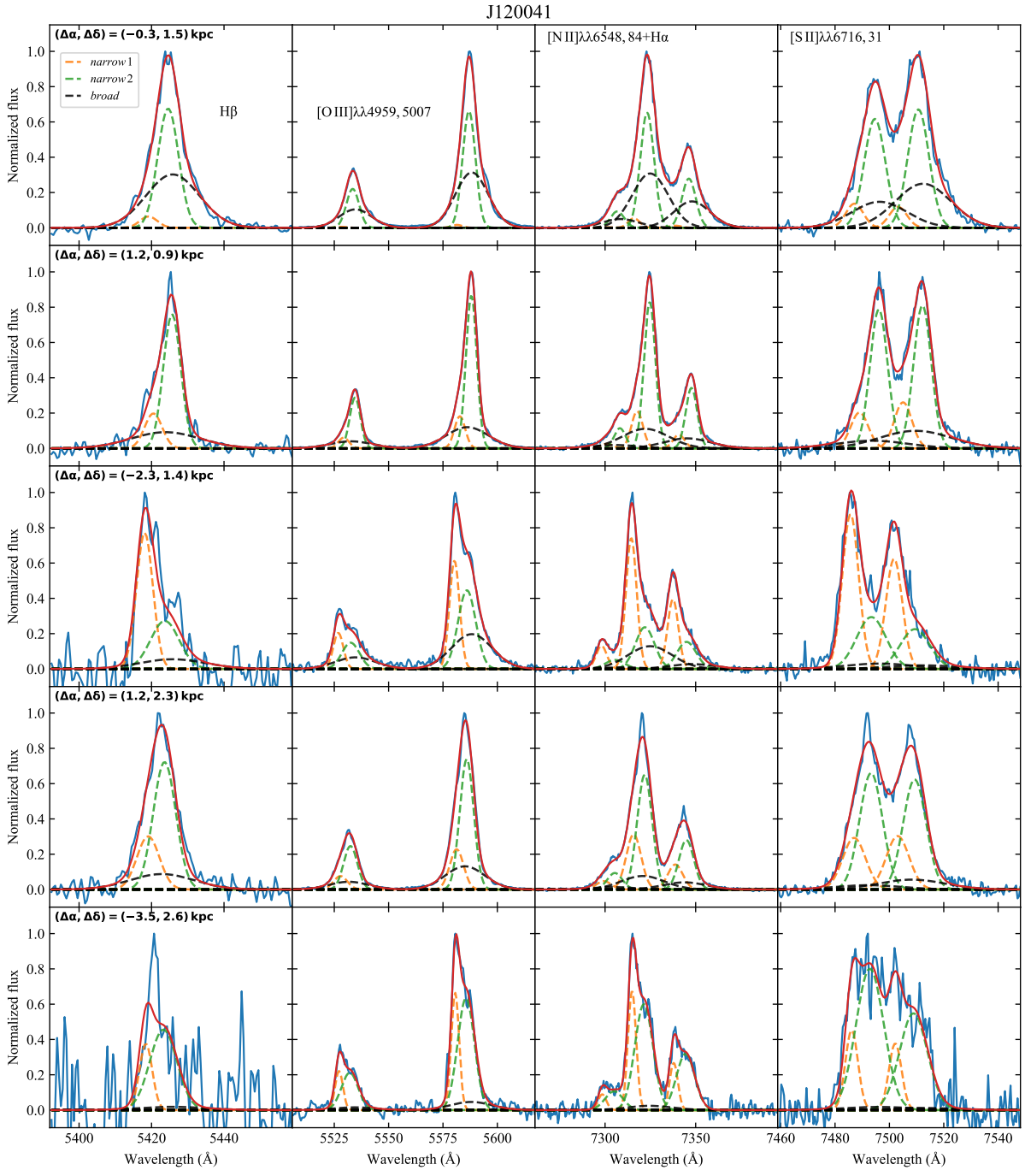

Figura 18 – Same as Fig. 19 but for J120041.

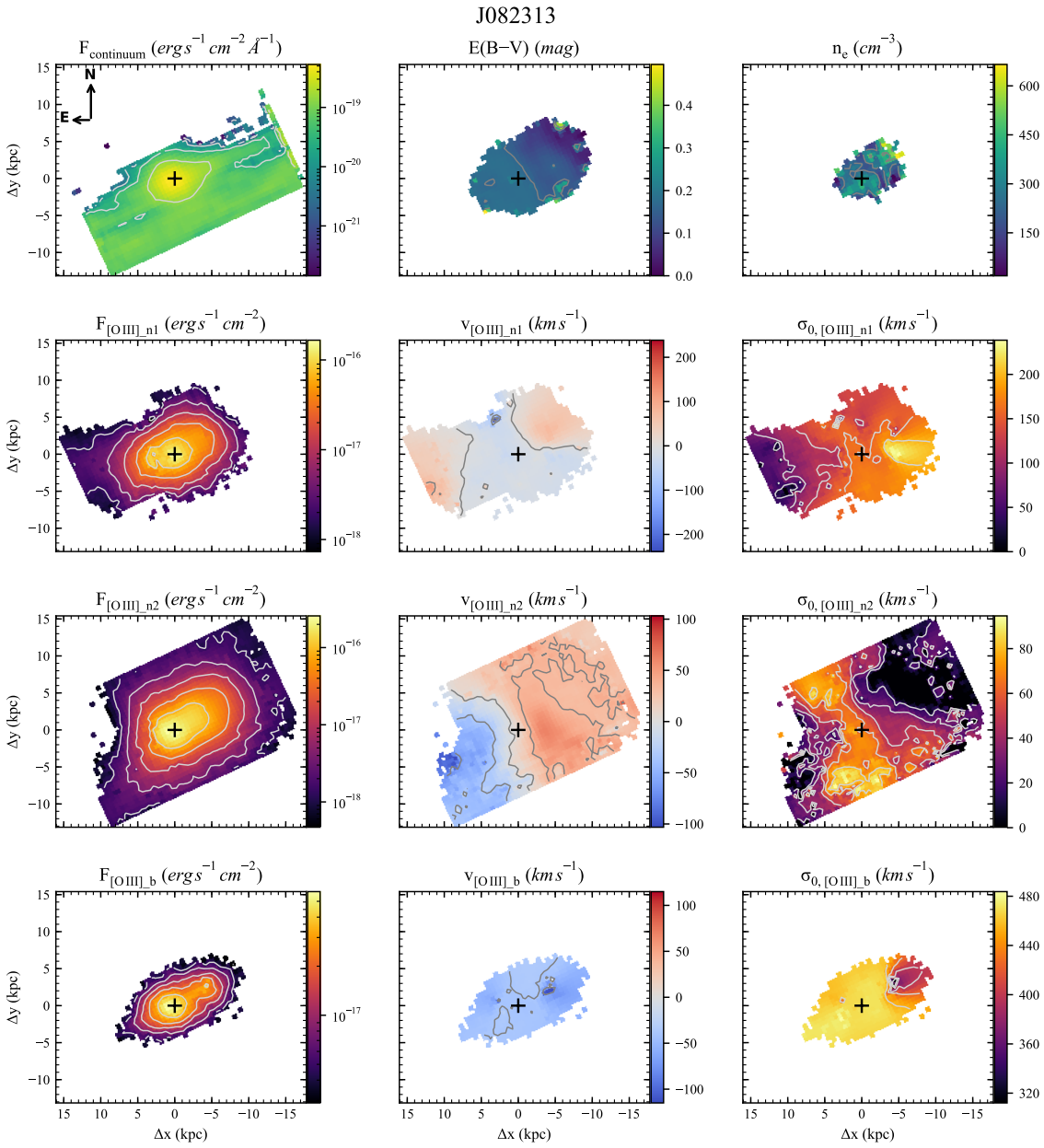

Figura 19 – Maps of J082313, similar to Fig. 7. In the first row, we have the continuum around the rest wavelength λ5600Å, the gas reddening, and the electron density maps. The rows below display the parameters of each component of [O III]λ5007: the left column accounts for the flux of each component; the middle, for the radial velocity; and the right column, the velocity dispersion. The last row refers to the *broad* component, that is modelling the outflow. The remaining middle columns refer to the *narrow* components.

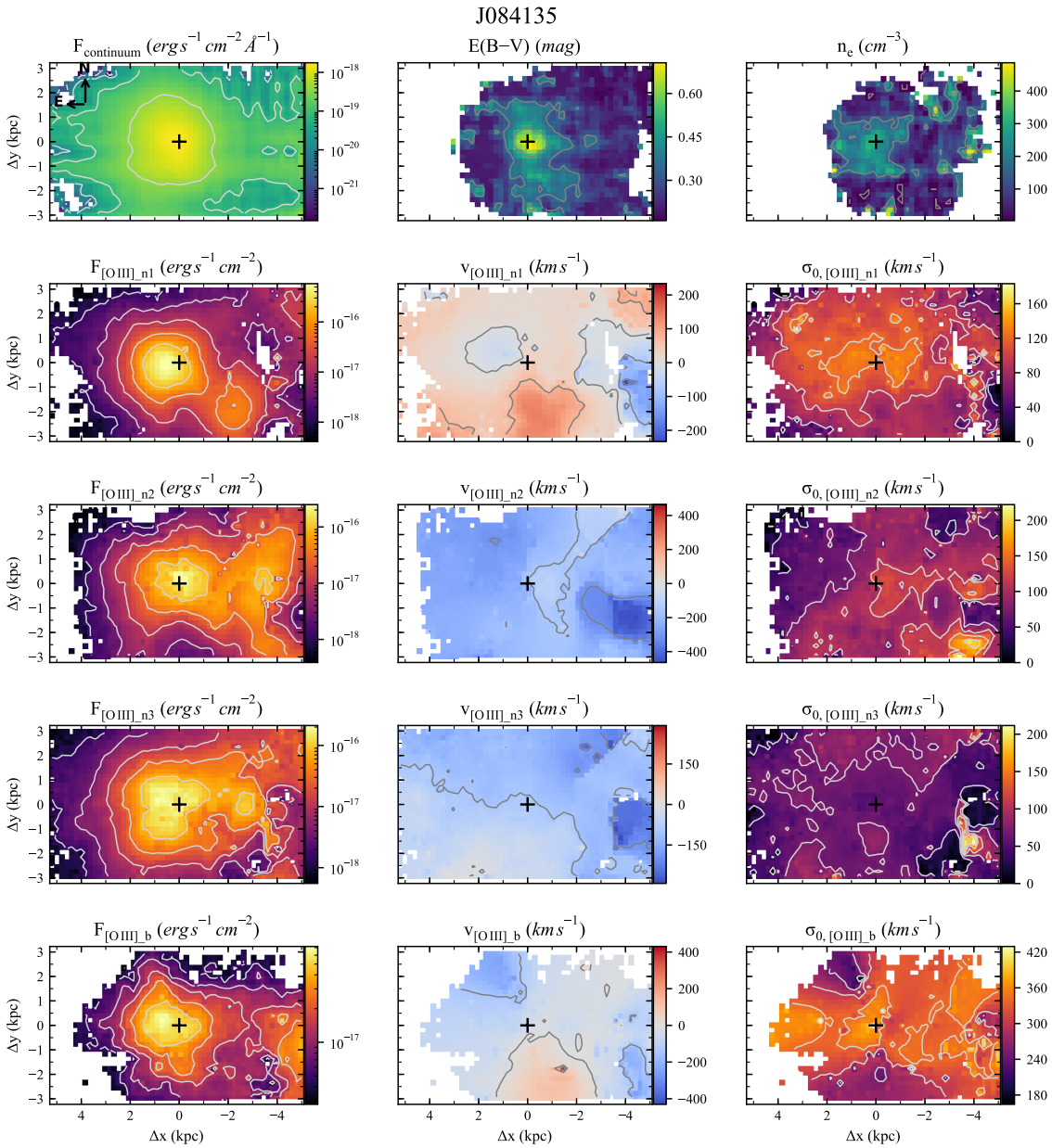

Figura 20 – Same as Fig. 19 but for J084135.

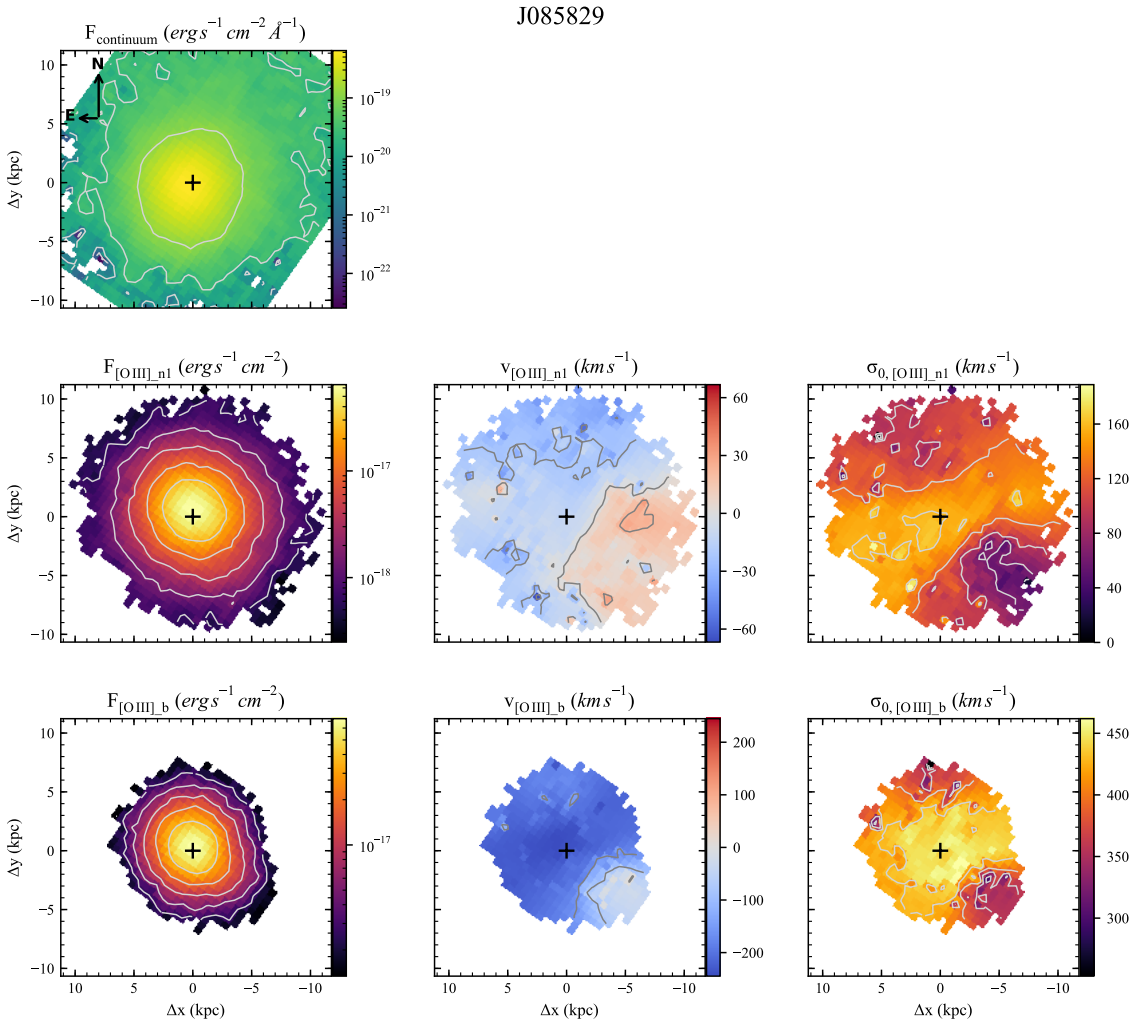

Figura 21 – Same as Fig. 19 but for J085829.

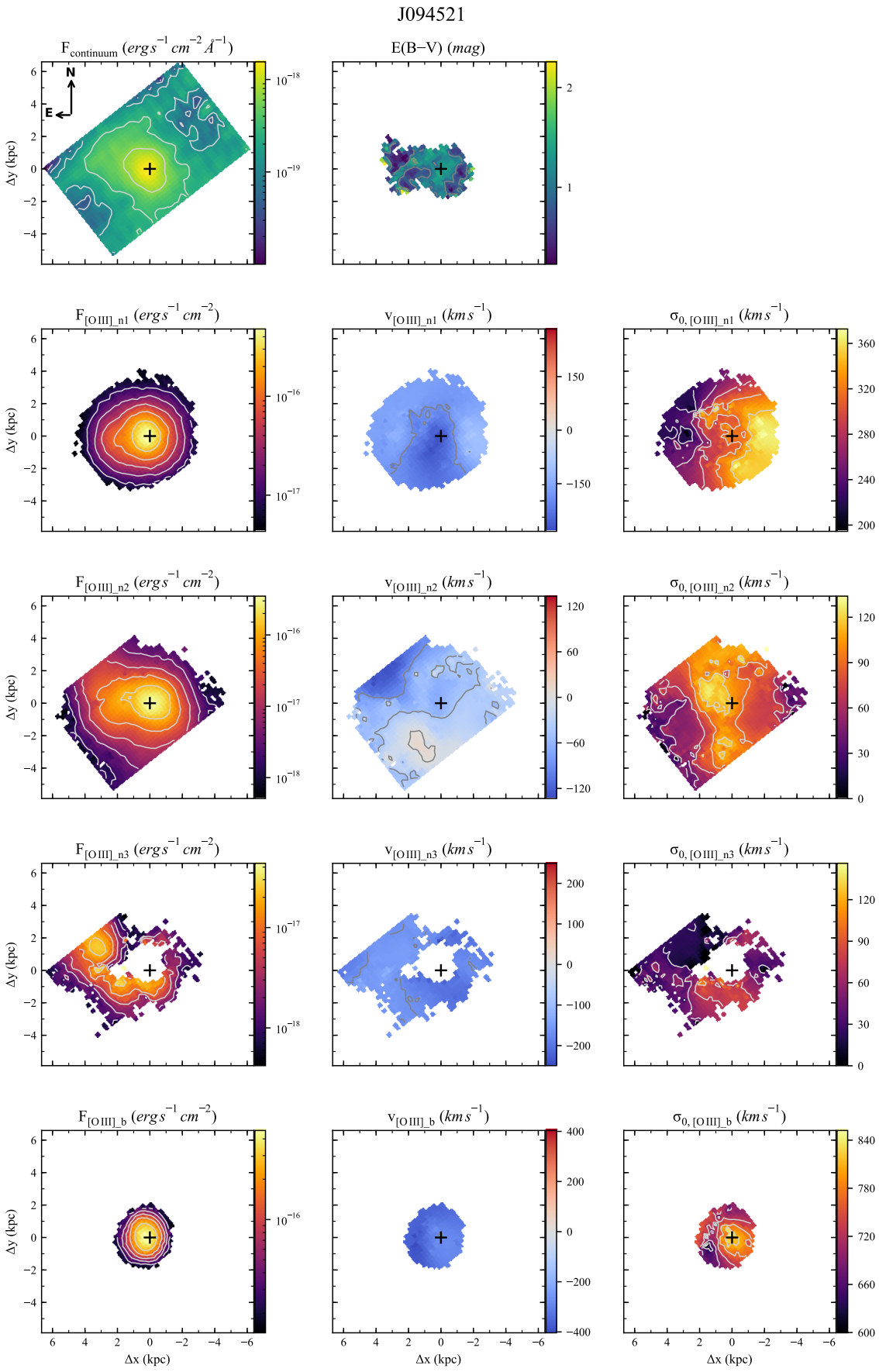

Figura 22 – Same as Fig. 19 but for J094521.

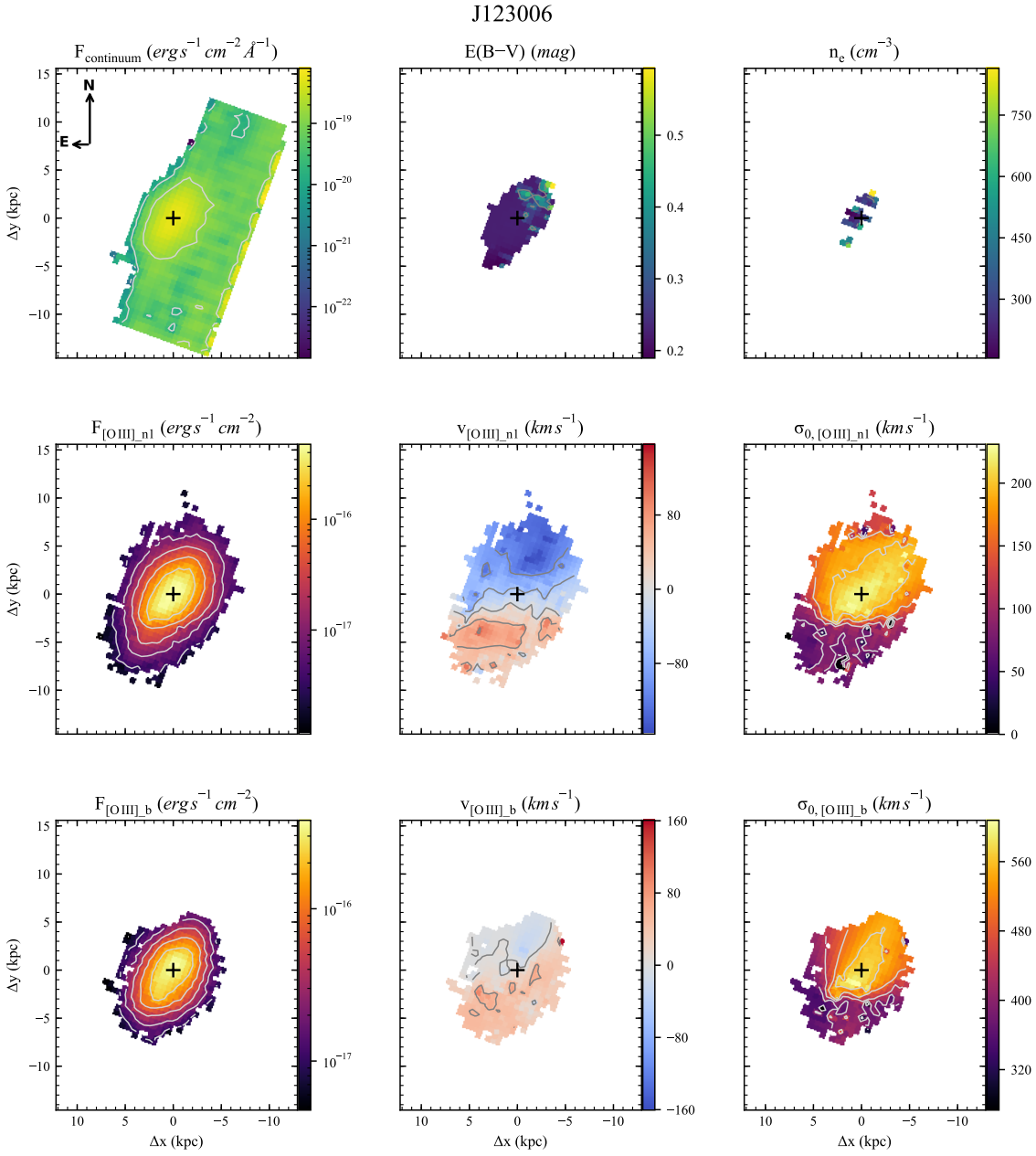

Figura 23 – Same as Fig. 19 but for J123006.

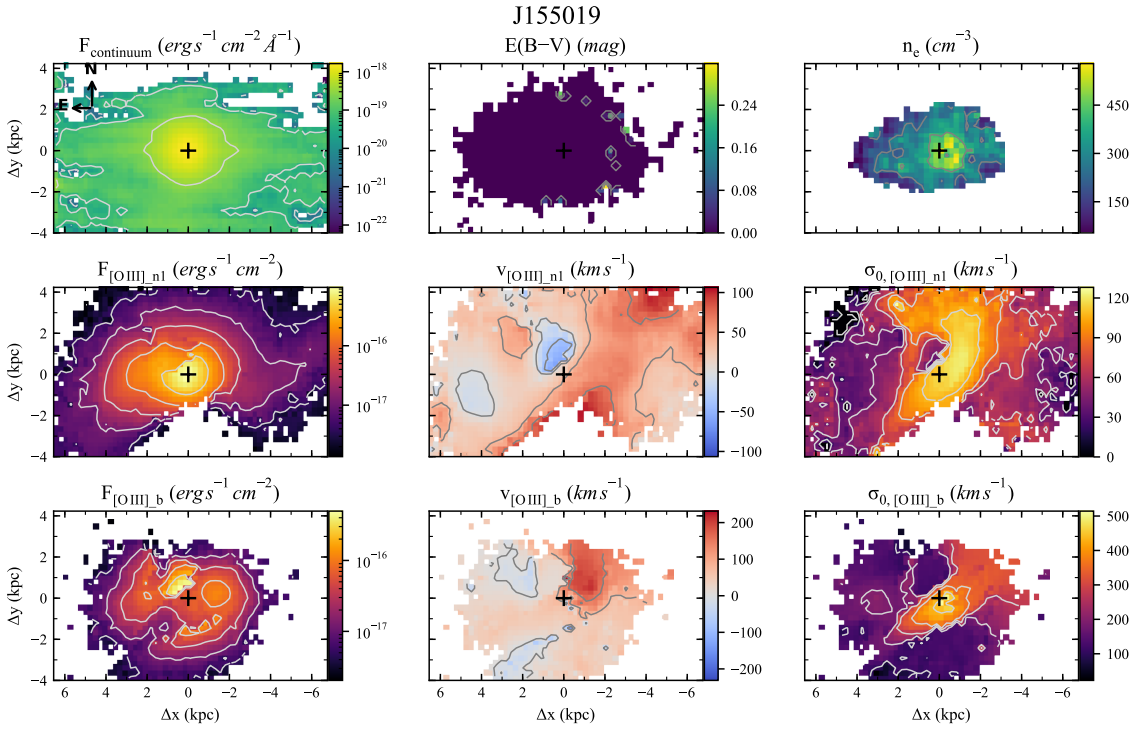

Figura 24 – Same as Fig. 19 but for J155019.

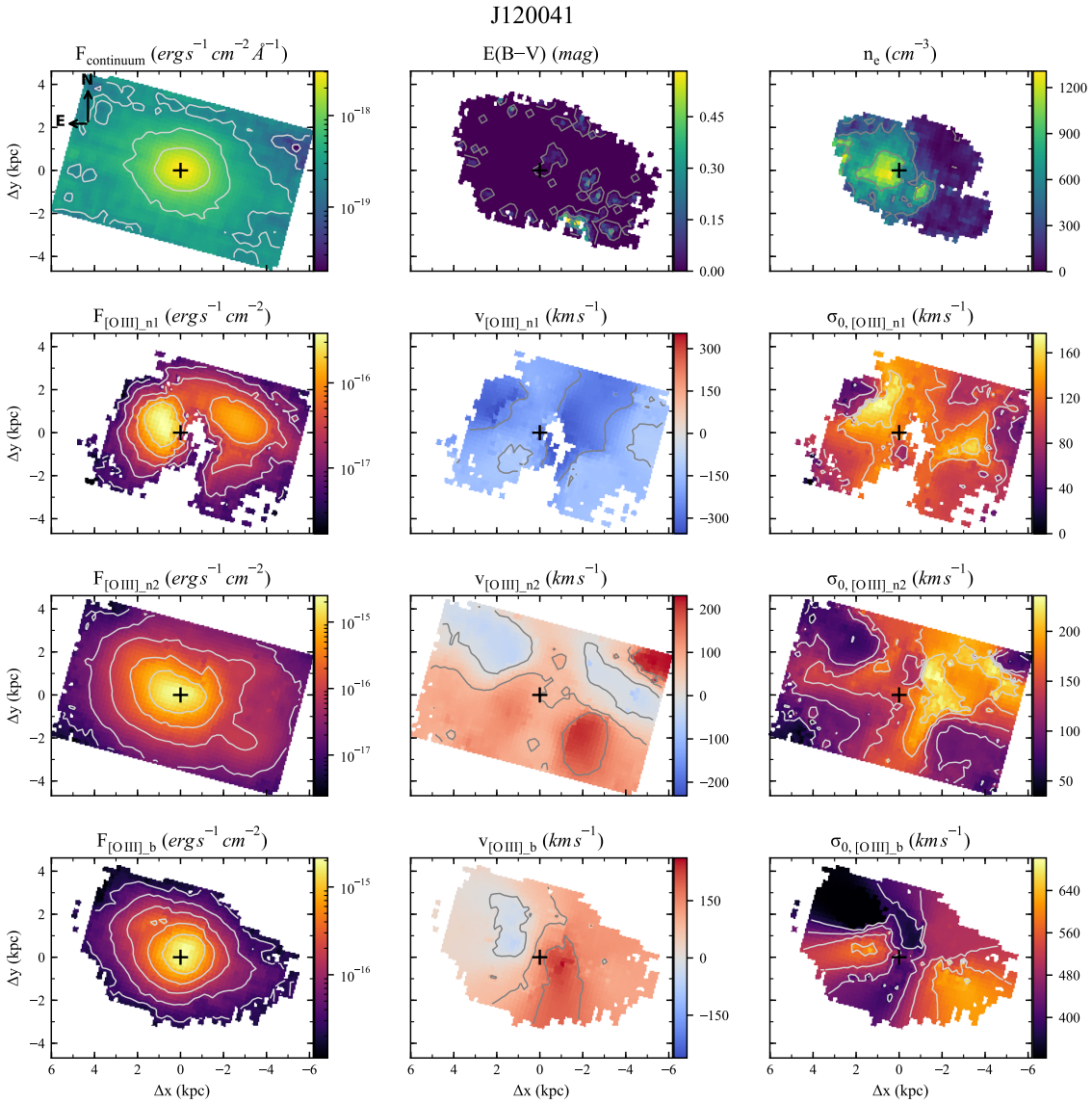

Figura 25 – Same as Fig. 19 but for J120041.